



Since January 2020 Elsevier has created a COVID-19 resource centre with free information in English and Mandarin on the novel coronavirus COVID-19. The COVID-19 resource centre is hosted on Elsevier Connect, the company's public news and information website.

Elsevier hereby grants permission to make all its COVID-19-related research that is available on the COVID-19 resource centre - including this research content - immediately available in PubMed Central and other publicly funded repositories, such as the WHO COVID database with rights for unrestricted research re-use and analyses in any form or by any means with acknowledgement of the original source. These permissions are granted for free by Elsevier for as long as the COVID-19 resource centre remains active.



Research paper

Repurposing 1,2,4-oxadiazoles as SARS-CoV-2 PLpro inhibitors and investigation of their possible viral entry blockade potential

Mohammed Salah Ayoup^{a,*}, Mariam M. ElShafey^a, Hamida Abdel-Hamid^a, Doaa A. Ghareeb^b, Marwa M. Abu-Serie^c, Lamia A. Heikal^d, Mohamed Teleb^e

^a Department of Chemistry, Faculty of Science, Alexandria University, Alexandria, 21321, Egypt

^b Bio-screening and preclinical trial lab, Biochemistry Department, Faculty of Science, Alexandria University, P.O. Box 21511, Alexandria, Egypt

^c Medical Biotechnology Department, Genetic Engineering and Biotechnology Research Institute, City of Scientific Research and Technological Applications (SRTA-City), Egypt

^d Department of Pharmaceutics, Faculty of Pharmacy, Alexandria University, Alexandria, 21521, Egypt

^e Department of Pharmaceutical Chemistry, Faculty of Pharmacy, Alexandria University, Alexandria, 21521, Egypt

ARTICLE INFO

Keywords:

SARS-CoV-2

PLpro

Spike RBD

1,2,4-Oxadiazole

ABSTRACT

Although vaccines are obviously mitigating the COVID-19 pandemic diffusion, efficient complementary antiviral agents are urgently needed to combat SARS-CoV-2. The viral papain-like protease (PLpro) is a promising therapeutic target being one of only two essential proteases crucial for viral replication. Nevertheless, it dysregulates the host immune sensing response. Here we report repositioning of the privileged 1,2,4-oxadiazole scaffold as promising SARS-CoV-2 PLpro inhibitor with potential viral entry inhibition profile. The design strategy relied on mimicking the general structural features of the lead benzamide PLpro inhibitor GRL0617 with isosteric replacement of its pharmacophoric amide backbone by 1,2,4-oxadiazole core. Inspired by the multitarget antiviral agents, the substitution pattern was rationalized to tune the scaffold's potency against other additional viral targets, especially the spike receptor binding domain (RBD) that is responsible for the viral invasion. The Adopted facial synthetic protocol allowed easy access to various rationally substituted derivatives. Among the evaluated series, the 2-[5-(pyridin-4-yl)-1,2,4-oxadiazol-3-yl]aniline (**5**) displayed the most balanced dual inhibitory potential against SARS-CoV-2 PLpro ($IC_{50}=7.197\ \mu M$) and spike protein RBD ($IC_{50}=8.673\ \mu M$), with acceptable ligand efficiency metrics, practical LogP (3.8) and safety profile on Wi-38 ($CC_{50}=51.78\ \mu M$) and LT-A549 ($CC_{50}=45.77\ \mu M$) lung cells. Docking simulations declared the possible structural determinants of activities and enriched the SAR data for further optimization studies.

1. Introduction

SARS-CoV-2 continues to spread worldwide despite the global vaccination campaign exceeding 11 billion administered doses [1]. While vaccines are considered the central pillar of our efforts to fight against COVID-19 pandemic [2], small-molecule antiviral agents should maintain a complementary therapeutic approach [3]. Since the early stages of COVID-19 pandemic, various drug discovery pipelines were deployed to identify chemical entities inhibiting SARS-CoV-2, its etiologic agent. Several viral proteins have been validated as druggable therapeutic targets [4–6]. Of which, the main protease (Mpro), the RNA-dependent RNA polymerase (RdRp), and the Papain-like protease (PLpro), have received significant attention. Accordingly, Pfizer have

developed the Mpro inhibitor nirmatrelvir [7]. Simultaneously, Merck developed molnupiravir, targeting the RdRp [8], another small-molecule anti-COVID-19 agent. Despite these groundbreaking therapeutic options, subsequent studies showed that these antiviral agents demonstrated subpar pharmacological properties [9,10]. Although the viral Mpro and RdRp have been well studied, there is an eager need to investigate the other potential SARS-CoV-2 constituents such as the PLpro, especially in case of Mpro or RdRp develops resistant mutations under the current therapeutic pressure [11,12]. Most recently, SARS-CoV-2 resistance to nirmatrelvir has been reported via multiple pathways [13]. Several drug resistant hot spots were identified due to mutations impacting the conformational stability of the active site [14]. Such mutations observed could form a strong foundation to

* Corresponding author.

E-mail address: Mohamed.salah@alexu.edu.eg (M.S. Ayoup).

<https://doi.org/10.1016/j.ejmech.2023.115272>

Received 19 December 2022; Received in revised form 3 March 2023; Accepted 8 March 2023

Available online 13 March 2023

0223-5234/© 2023 Elsevier Masson SAS. All rights reserved.

inform the design of next-generation protease inhibitors. It is worth mentioning that several updated reviews highlighted the major achievements in structure-based design and high-throughput screening of lead SARS-CoV-2 PLpro inhibitors [15–17]. It is expected that potential PLpro inhibitors combined with other directed antiviral agents will present viable therapeutic option to surmount the COVID-19 drug resistance [18] based on lessons learned from synergistic antiviral cocktails effective against numerous viruses such as HIV [19]. Consequently, interest in PLpro has obviously grown as the next major SARS-CoV-2 therapeutic target.

Several studies showed that SARS-CoV-2 PLpro suppresses the host innate immune responses and process the viral polyproteins ensuring viral proliferation and replication [20]. Mechanistically, PLpro is characterized by deISGylating and deubiquitinating activities [21] that interferes with the release of necessary interferons to upregulate the antiviral cytokines production and instigate the host immune responses [22]. Substantial SARS-CoV-2-related mortality is associated with cytokine storms that arise from these dysregulated responses [23]. PLpro also cleaves the SARS-CoV-2 polyproteins into nonstructural proteins that are required for virus replication and RNA transcription [24]. This dual role relies on the enzymatic binding capacity to both the

host and viral proteins via its active site. Therefore, developing small-molecules that block PLpro active site should effectively inhibit the enzyme in a ‘two birds, one stone’ scenario [25]; restoring the natural host defense mechanism and blocking the viral replication. One of the most studied lead SARS-CoV-2 PLpro inhibitors is GRL0617, a noncovalent binder that was previously developed for SARS-CoV-1 PLpro in 2008 [26]. Due to the fact that both PLpro from SARS-CoV-1 and SARS-CoV-2 share several structural features, GRL0617 unsurprisingly maintained its inhibitory potency against SARS-CoV-2 PLpro with low range micromolar IC_{50} [21]. Crystallization of SARS-CoV PLpro with GRL0617 revealed that key viral residues and the structural determinants of inhibitor’s activity [26,27]. The scaffold of GRL0617 thus represented a challenging starting point for further optimization studies and encouraged several design strategies to seek out new PLpro hits [28]. Many GRL0617 analogs have been introduced (Fig. 1), even though no inhibitor has been approved by the FDA. Osipiuk *et al.* reported a series of GRL0617 analogs [29]. However, none of them surpassed GRL0617. Later, Ma *et al.* succeeded to develop two inhibitors, Jun9-13-7 and Jun9-13-9, equipotent to GRL0617 [30]. Interestingly, further optimization studies afforded Jun9-72-2 (IC_{50} = 0.67 μ M) and Jun9-75-4 (IC_{50} = 0.62 μ M) with higher potency compared to GRL0617.

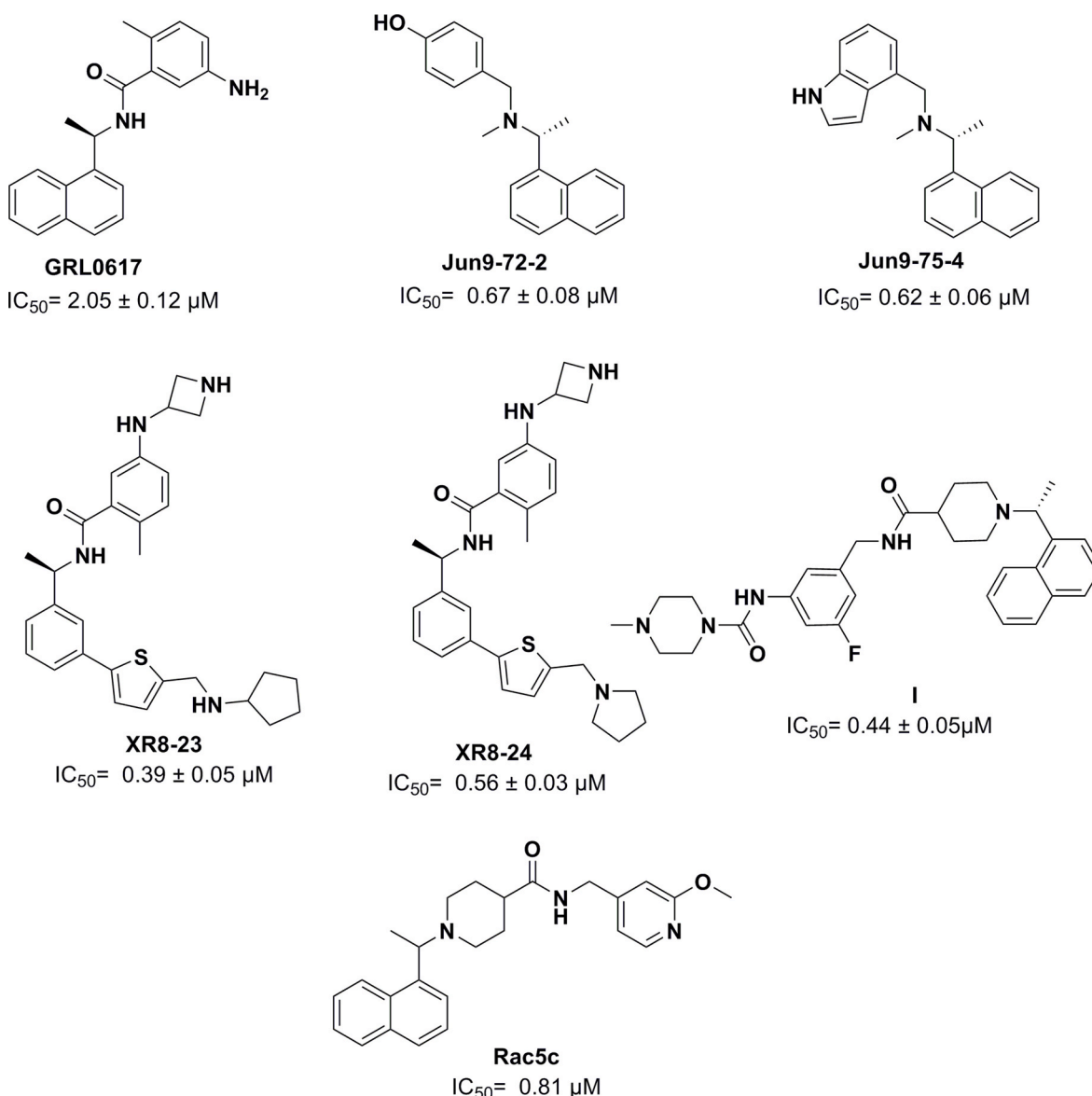


Fig. 1. Lead PLpro inhibitors.

Jun9-72-2 adopts similar binding mode with PLpro as GRL0617. Shan *et al.* then focused on structure-based optimization of GRL0617 and introduced the superior PLpro inhibitor **I** with promising PLpro inhibitory profile ($IC_{50} = 0.44 \mu M$) and antiviral activity against SARS-CoV-2 ($IC_{50} = 0.18 \mu M$) [31]. Moreover, **I** showed no significant cross-inhibition against another 10 deubiquitinating enzymes (DUB) or DUB-like proteases even at $10 \mu M$ [31]. Collectively, **I** is a promising SARS-CoV-2 PLpro inhibitor in virtue of its potency and selectivity. Other previously identified naphthalene-based inhibitors, namely, Rac3j, Rac3k, and Rac5c, also showed promising inhibitory activities against SARS-CoV-2 PLpro. Rac5c was the most potent among the group with IC_{50} value of $0.81 \mu M$ [32]. In the antiviral assay, Rac5c protected SARS-CoV-2 infected Vero cells from the cytopathic effects without toxicity at $11 \mu M$, Shen *et al.* explored the engagement of additional binding sites to GRL0617 [33]. ZN-2-184, a GRL0617 derivative with azetidine substitution on the phenyl ring, yielded a 2-fold improved affinity to PLpro. ZN-3-80, a ZN-2-184 derivative with a biaryl group instead of the naphthyl group, showed improved metabolic stability compared to GRL0617. Further exploration of ZN-3-80 led to the newly synthesized 2-phenylthiophene derivatives, XR8-23 and XR8-24, displaying submicromolar potency against SARS-CoV-2 PLpro ($IC_{50} = 0.39$ and $0.56 \mu M$, respectively) and low micromolar potency against A549 infected cells ($EC_{50} = 1.4$ and $1.2 \mu M$, respectively) surpassing GRL0617. Furthermore, both compounds showed satisfactory bioavailability profiles in mouse model [33].

2. Design rationale

In the current work, we set out our research protocol to explore the PLpro inhibitory potential of rationally designed 2,5-diaryl-1,2,4-oxadiazoles investing the facial synthesis and easy access to this privileged scaffold. Accordingly, we first selected the naphthalenyl benzamide PLpro inhibitor GRL0617 as our lead scaffold, based on its superior potency relative to other identified hits, and the availability of the viral PLpro: GRL0617 cocrystal structure (PDB: 3E9S [34]) that will guide docking simulations and enrich the structural determinants of activity. The pharmacophoric amide backbone of GRL0617 was then replaced by 1,2,4-oxadiazole core being its non-classical isostere [35, 36], while keeping the aromatic termini resembling the general theme of GRL0617 (Fig. 2). The substitution pattern of the installed aryl groups was directed as possible to mimic GRL0617 and other lead inhibitors.

The therapeutic benefits of combination studies [18,19,37,38] sparked our interest to probe the target compounds' activities against other important viral targets including the spike receptor binding domain (RBD) that links with human angiotensin-converting enzyme 2 (hACE2) receptor allowing viral invasion [39,40]. It is worth mentioning that the virus-host engagement is generally dominated by polar contacts mediated by the key hydrophilic amino acid residues within the spike RBD and hACE2 [40]. Accordingly, Sarafianos *et al.* identified an oxazole-carboxamide derivative, SSAA09E2, that blocks the binding of the viral RBD and ACE2 with $IC_{50} = 3.1 \mu M$ [41]. Chloroquine ($IC_{50} = 1.13 \mu M$) [42], hydroxychloroquine ($IC_{50} = 0.72 \mu M$) and the flavanone glycoside hesperidin [43,44] were also repurposed for SARS-CoV-2 entry blockade. This consideration directed our design

approach to incorporate versatile polar moieties to aromatic termini of the target 1,2,4-oxadiazole-based scaffold to allow fine tuning of dual possible PLpro-spike protein blockade.

3. Results and discussion

3.1. Chemistry

A novel series of 3,5-disubstituted-1,2,4-oxadiazole containing mono- or disubstituted **4–10**. These varieties of the novel 1,2,4-oxadiazole derivatives were prepared as described in Scheme 1 via the reaction of the corresponding nitrile namely 2-hydroxybenzonitrile, 2-amino-benzonitrile, benzonitrile, or *p*-trifluoromethylbenzonitrile **1a–d**, respectively with hydroxylamine solution in ethanol affording the corresponding amidoxime **2a–d**. Consequently, condensation of the amidoxime **2a–d** with ethyl salicylate, isonicotinate, or anthranilate utilizing NaOH/DMSO protocol afforded the respective 3,5-disubstituted-1,2,4-oxadiazole **4–10** in excellent yields (Scheme 1). The structures of all the prepared target compounds **4–10** were confirmed by spectral analyses, where the 1H NMR showed characteristic signals for the NH_2 groups at chemical shift range 6.31–6.98 ppm, whereas the ^{13}C NMR spectra confirmed the presence of oxadiazole carbons at 175–166 ppm.

Regarding compound **8**, the presence of two OH groups was confirmed by IR and 1H NMR spectra. The IR spectra of **8** showed broad band at 3333 cm^{-1} characteristic to OH groups. The 1H NMR spectrum in DMSO- d_6 solution clearly showed the characteristic signals for the OH protons at (δ_H) 10.71 and 10.16 ppm of two protons intensity indicating the presence of two phenolic OH groups. In ^{13}C NMR spectrum, the duplicate signals of **8** might be attributed to the possible existence of different arrangement of hydrogen bonds (one hydrogen bond in **11** and/or two hydrogen bond in **12**) between the OH and the nitrogen atom of the oxadiazole ring that has pyridine-like lone pair of electron as illustrated in Fig. 3 [45]. Where, the carbons of the oxadiazole ring appeared at (δ_C) 174.1, 166.4 (2C), 163.7 ppm which means that compound **8** is present in two different forms. In ^{13}C NMR spectrum of compound **9**, the trifluoromethyl group carbon appeared at δ_C 128.6 ppm.

Furthermore in Scheme 2, functionalization of the novel 3,5-disubstituted-1,2,4-oxadiazoles was accomplished by reflux the novel 1,2,4-oxadiazole **4** or **10** with monosodium salt of pyridoxal-5'-phosphate (P5P), the active form of vitamin B6 affording the corresponding Schiff's bases **13** and **14**, respectively. The structures of compounds **13** and **14** were confirmed by spectral analyses where ^{13}C NMR of **13** showed signals at 62.0 and 18.9 ppm correspond to CH_2 and CH_3 , respectively. Moreover, the 1H NMR spectrum of **13** showed characteristic phenolic OH at δ_H 9.3 ppm and acidic proton of the phosphate group at δ_H 13.2 ppm. The 1H NMR of **14** showed a characteristic peak of the phenolic OH at δ_H 9.4 ppm and acidic proton at δ_H 13.3 ppm, respectively. The two Schiff's bases appeared in the (*E*) form.

The preparation of the target disubstituted 1,2,4-oxadiazoles **15–19** were accomplished by the transformation of both OH and NH_2 of compound **4** to other versatile function groups by treating **4** with different reagents as described in Scheme 3, where acylation of **4** via refluxing in

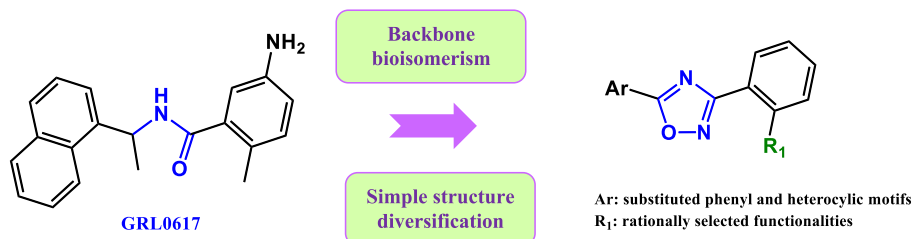
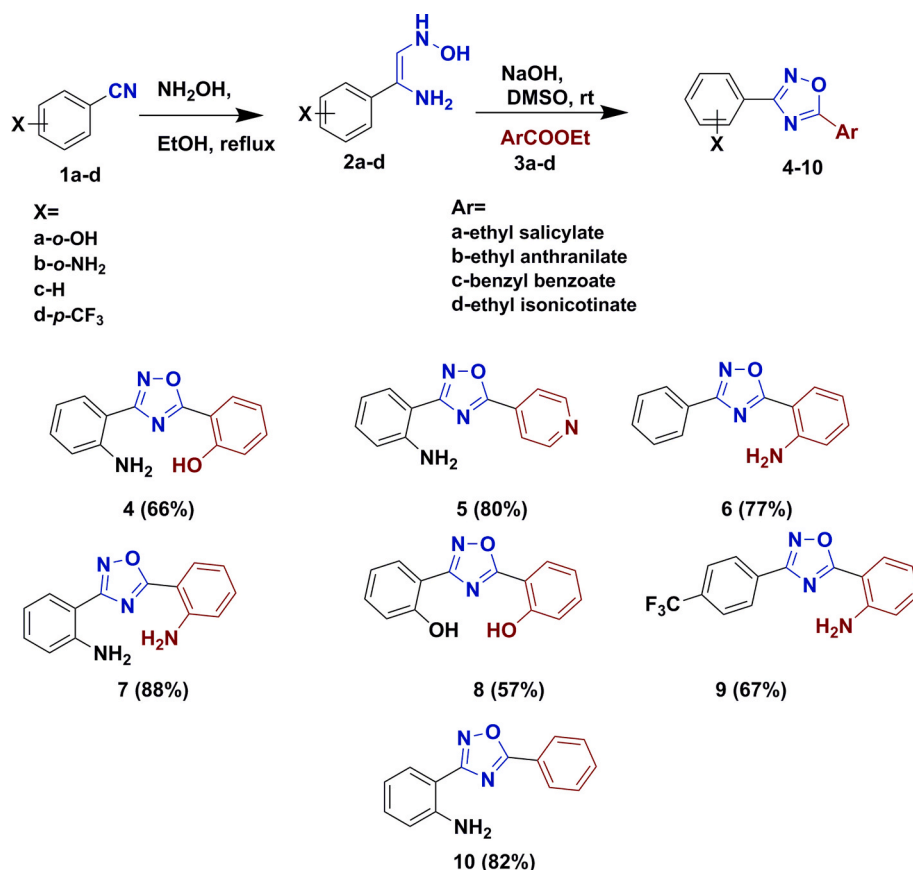


Fig. 2. Design rationale of the target oxadiazoles.



Scheme 1. Synthesis of novel 3,5-disubstituted-1,2,4-oxadiazole 4–10.

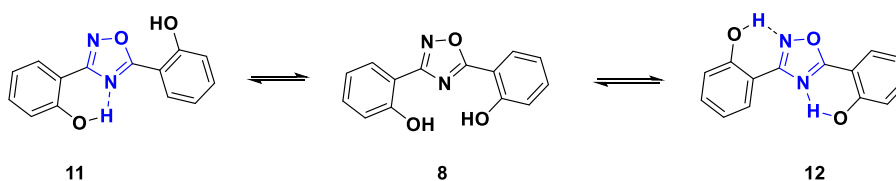


Fig. 3. The hydrogen bonds arrangement in compound 8.

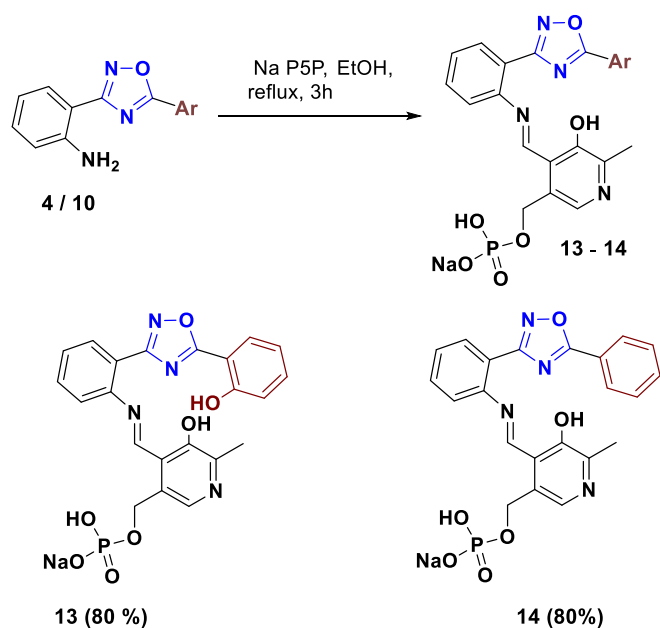
acetic anhydride afforded the peracetylated derivative **15**. Its ^1H NMR spectrum showed three acetyl group at (δ_{H}) 2.37 & 2.14 ppm. Furthermore, diazotization of **4** utilizing sodium nitrite/AcOH protocol followed by treatment of the formed diazonium salt with sodium azide afforded the corresponding aromatic azido derivative **16**. The IR of **16** showed characteristic band at 2131, and 2096 cm^{-1} revealing to the azido group. Its ^1H NMR lacked the NH_2 signal at (δ_{H}) 6.32 ppm. Alternatively, formylation of **4** with formic acid under reflux for 2 h afforded the corresponding *N*-formyl derivative **17** in 85% yield. The IR spectrum of **17** showed absorption band at 1710 cm^{-1} for the amide carbonyl group. The ^1H NMR spectrum in $\text{DMSO}-d_6$ solution showed the characteristic signal for the OH proton at (δ_{H}) 10.72 ppm of one proton intensity and the signal for the HCON proton at (δ_{H}) 10.17 ppm. The ^1H NMR showed also showed a characteristic signal at (δ_{H}) 8.47 ppm for CHO. On the other hand, alkylation via nucleophilic substitution reaction of **4** using ethyl bromoacetate utilizing K_2CO_3 anhydrous as catalyst in DMF under reflux for 24 h afforded the unexpected polycyclic product **18** rather than the expected diester product **20**. It's IR spectrum showed a characteristic absorption band at 1768 cm^{-1} for the ester carbonyl group and amidic carbonyl absorption was assigned at 1650 cm^{-1} . The ^1H NMR spectrum of **18** showed a signal at (δ_{H}) 5.71 ppm due to CH_2 , doublet of doublet at (δ_{H}) 4.16 and 3.85 ppm due to CH_2 and singlet at

(δ_{H}) 1.2 ppm due to CH_3 protons. The IR and ^1H NMR spectra of the unexpected polycyclic compound **18** confirmed the success of the intramolecular cyclization reaction by the disappearance of the signals corresponding to OH and NH_2 protons and the appearance of the signals at (δ_{H}) 5.71, 3.9 and 1.2 ppm assigned to the methylene and ethyl groups. Furthermore, the saponification of **18** utilizing sodium hydroxide afforded the corresponding free acid **19**, where the IR spectrum showed characteristic absorption band at 1788 cm^{-1} for carbonyl group besides the amidic carbonyl absorption at 1688 cm^{-1} . The ^1H NMR spectrum of **19** showed signals at (δ_{H}) 4.94 and 4.09 ppm assigned to the methylene groups, and a broad singlet band at (δ_{H}) 13.03 ppm due to OH, at which the disappearance of ethyl group protons and the concealing of ethyl ester group replacing it with one proton proved our structure.

3.2. Biology

3.2.1. Cytotoxicity screening

The cytotoxic effects of the synthesized oxadiazoles **4–19** were tested by determining the maximal effective concentration (EC_{100}), representing the safe dose, and the 50% cytotoxic concentration (CC_{50}) for each compound against normal human lung fibroblast (Wi-38) cell line



Scheme 2. Synthesis of sodium salt of P5P Schiff's bases of the disubstituted 1,2,4-oxadiazole (13 and 14).

and long-term cultivated human lung cancer cell line (LT-A549) after 72 h incubation (Table 1). The latter cell line was utilized as a model for alveolar epithelial type II (ATII) which is the main target cell of SARS2-CoV-2. LT-A549, upon its cultivation in Ham's F12 medium for a long term (25 days), represents a more suitable source of functional ATII cells [46,47]. Interestingly, most of the studied compounds displayed $EC_{100} > 4 \mu M$. 6 exhibited the highest safety profile ($EC_{100} = 19.06 \mu M$) against Wi-38, followed by 5 ($EC_{100} = 10.36 \mu M$), 7 ($EC_{100} = 9.74 \mu M$) and 17 ($EC_{100} = 8.12 \mu M$). Other derivatives were relatively less safe with EC_{100} ranging from 7.70 to 0.64 μM . On the other hand, 17 surpassed the other derivatives regarding safety against LT-A549 with $EC_{100} = 15.71 \mu M$, followed by 7 ($EC_{100} = 12.25 \mu M$), 6 ($EC_{100} = 11.68$

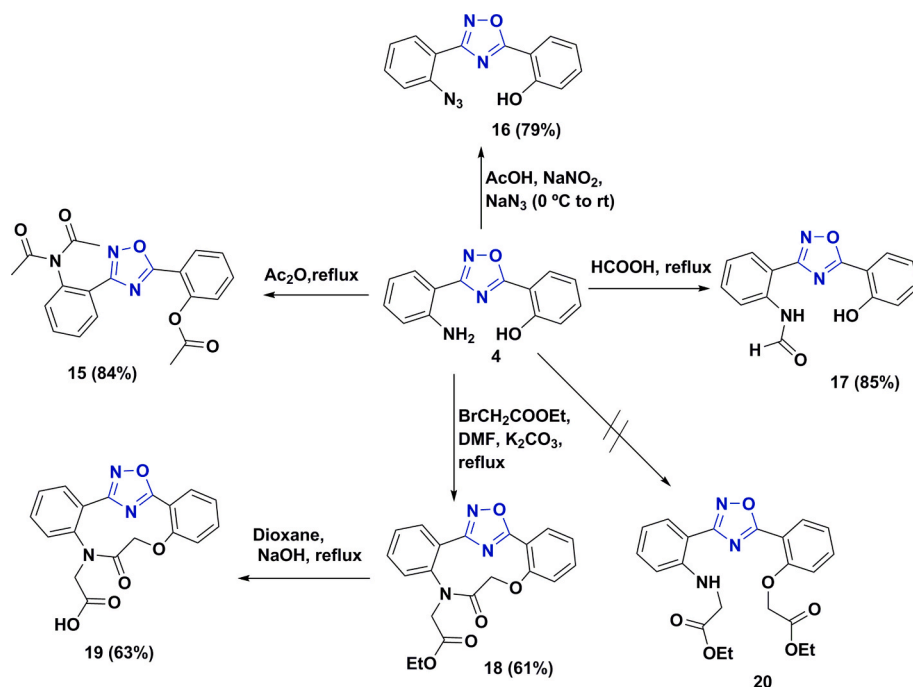
μM) and 5 ($EC_{100} = 8.35 \mu M$), whereas the remainders recorded EC_{100} within 7.13 and 0.21 μM . The highest 50% cytotoxic concentrations against Wi-38 were recorded by 6 ($CC_{50} = 57.17 \mu M$), 5 ($CC_{50} = 51.78 \mu M$) and 7 ($CC_{50} = 48.69 \mu M$). 17 ($CC_{50} = 40.57 \mu M$), 16 ($CC_{50} = 38.50 \mu M$) and 10 ($CC_{50} = 36.49 \mu M$) were moderately safe, whereas other derivatives exhibited relatively lower CC_{50} values ranging from 32.36 to 3.20 μM . Assessment of CC_{50} against LT-A549 revealed that 5 was the safest oxadiazole derivative with $CC_{50} = 45.77 \mu M$, followed by 17 ($CC_{50} = 31.43 \mu M$), 7 ($CC_{50} = 28.97 \mu M$), 10 ($CC_{50} = 28.71 \mu M$) and 16 ($CC_{50} = 28.22 \mu M$). The remainder derivatives recorded CC_{50} within the range 24.66–1.03 μM .

3.2.2. SARS-CoV-2 papain-like proteinase (PLpro) inhibitory activities

% Inhibition of SARS-CoV-2 PLpro was determined for all the newly synthesized oxadiazole derivatives 4–19 at 10 μM (Table 2) as previously reported [48]. Among the evaluated derivatives, 5 recorded the highest % inhibition (58.6%). Compounds 17, 14, 6 and 10 were moderately active against PLpro with % inhibition 35.1, 22.5, 21.1 and 20.8%, respectively. The other derivatives exhibited relatively lower activities. According to the SARS-CoV-2 PLpro inhibitory activities results, we opted to further determine the IC_{50} value of the oxadiazole derivative 5 against PLpro. Interestingly, it demonstrated an IC_{50} of 7.197 μM , which was considered promising start point for further optimization when compared with the reported lead GRL0617 ($IC_{50} = 2.05 \mu M$) [49] and related inhibitors with micromolar IC_{50} values [34].

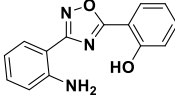
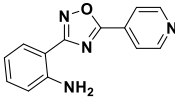
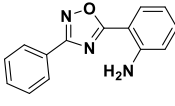
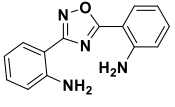
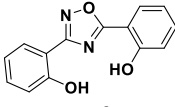
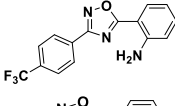
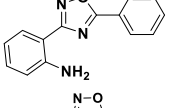
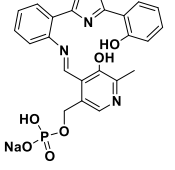
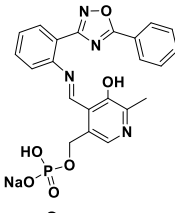
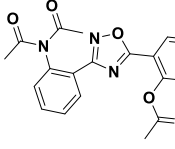
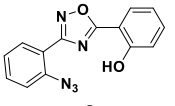
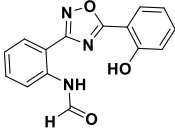
3.2.3. Spike protein receptor binding domain (RBD) inhibitory activities

All the studied oxadiazole derivatives 4–19 were screened for their potential to block the viral entry via inhibition of the activities against SARS-CoV-2 spike protein RBD at 10 μM (Table 3) as previously reported [48]. Again, 5 recorded the highest RBD % inhibition (65.6%) among all the evaluated derivatives, followed by 17 (44.4%), 15 (44.4%), 14 (36.7%), 6 (31.4%), respectively. The remainders were relatively less active. Further evaluation of 5 demonstrated that it exhibited IC_{50} of 8.673 μM , thus considered promising when compared with the reported reference inhibitor.



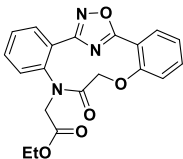
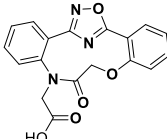
Scheme 3. Synthesis of 3,5-disubstituted 1,2,4-oxadiazoles (15-19).

Table 1
Safe concentrations (EC_{100} , μM) and 50% cytotoxic concentration (CC_{50} , μM) of the tested compounds after 72 h incubation with Wi-38 and LT-A549 cells.

Compound No.	Structure	Wi-38		LT-A549	
		EC_{100} (μM)	CC_{50} (μM)	EC_{100} (μM)	CC_{50} (μM)
4		6.474 ± 0.275	32.368 ± 1.374	4.114 ± 0.175	21.990 ± 0.739
5		10.356 ± 0.245	51.781 ± 1.227	8.352 ± 0.198	45.775 ± 0.154
6		19.059 ± 0.670	57.176 ± 2.011	11.681 ± 0.411	24.663 ± 2.920
7		9.738 ± 0.086	48.692 ± 0.431	12.25 ± 0.108	28.975 ± 0.871
8		5.208 ± 0.604	26.041 ± 3.020	3.360 ± 0.389	19.453 ± 0.645
9		1.156 ± 0.111	5.782 ± 0.554	0.373 ± 0.036	2.372 ± 0.290
10		7.299 ± 0.696	36.496 ± 3.481	5.886 ± 0.561	28.714 ± 3.642
13		4.956 ± 0.884	3.205 ± 0.003	2.718 ± 0.485	1.031 ± 0.071
14		2.030 ± 0.006	10.148 ± 0.031	0.655 ± 0.002	6.458 ± 0.226
15		0.641 ± 0.001	20.401 ± 0.042	0.207 ± 0.002	20.538 ± 1.400
16		7.701 ± 0.714	38.505 ± 3.572	6.707 ± 0.622	28.222 ± 8.871
17		8.116 ± 0.032	40.579 ± 0.163	15.708 ± 0.063	31.434 ± 1.327

(continued on next page)

Table 1 (continued)

Compound No.	Structure	Wi-38		LT-A549	
		EC ₁₀₀ (μM)	CC ₅₀ (μM)	EC ₁₀₀ (μM)	CC ₅₀ (μM)
18		6.313 ± 0.353	31.564 ± 1.765	7.127 ± 0.398	14.236 ± 0.524
19		5.727 ± 0.751	23.777 ± 1.102	3.695 ± 0.485	19.629 ± 0.037

All values are expressed as mean ± SEM.

3.2.4. Experimental octanol/water partition coefficient (LogP) and ligand efficiency metrics determination of the hit oxadiazole derivative 5

Being an important pharmacokinetic parameter in drug discovery, the octanol/water partition coefficient (LogP) of the hit oxadiazole derivative 5 was practically determined via the capacity factor calculation method [50,51] employing Reverse Phase-HPLC. LogP encodes molecular forces controlling the drug interactions with receptors and its transport through membranes thus defining its bioavailability profile. Results (Table 4) demonstrated that logP value of the oxadiazole derivative 5 (LogP = 3.8) obeyed Lipinski's parameters (LogP ≤ 5) [52]. Based on the practical LogP value, the ligand efficiency metrics of the hit oxadiazole derivative 5 were computed as previously reported [53–58] for assessing its lead- or drug-likeness. Interestingly, 5 fulfilled the acceptable value for LE (0.3) [53–55], scored lead-like LLE (≥ 3) [55,56,59], and the optimal LELP (−10 < LELP < 10 [55]).

3.3. Docking simulations

The binding modes with the viral papain-like protease (PLpro) (PDB ID: 3E9S [34]) and spike receptor-binding domain (PDB ID: 6LZG [60]) were explored via docking simulations to allow more in-depth understanding of the structural determinants of the hit oxadiazole derivative 5 activities.

3.3.1. Docking of the oxadiazole derivative 5 into papain-like protease

Docking simulations were performed by employing MOE 2019.102 [61,62]. The papain-like protease crystal structure was downloaded from the protein data bank complexed with a noncovalent inhibitor (PDB ID: 3E9S [26]), subjected to the MOE default “structure preparation” module after elimination of unwanted residues. The hit oxadiazole derivative 5 was built in silico, energy minimized, then docked into the co-crystallized inhibitor binding site of the prepared viral PLpro. The docking protocol adopted herein was validated by restoring the experimental interactions following docking the reference co-crystallized inhibitor ($\Delta G = -7.57$ kcal/mol) at RMSD < 2 Å. Results showed that the studied derivative, resided well into the inhibitor's binding site ($\Delta G = -6.00$ kcal/mol). Interestingly, among the best binding poses, our hit compound was able to share some essential interactions with the co-crystallized PLpro inhibitor. As illustrated (Fig. 4), the oxadiazole ring of 5 exhibited π - π interactions with Tyr265, whereas the 3-phenyl substituent of the oxadiazole ring was buried into the ligand binding site displaying H- π interactions with Gln270.

3.3.2. Docking of the oxadiazole derivative 5 into the spike protein receptor binding domain

The coordinates of SARS-CoV-2 spike (S) protein C-terminal domain (SARS-CoV-2-CTD), containing the receptor binding domain, complexed with the human ACE2 (hACE2) were retrieved from the protein data

bank (PDB ID: 6LZG [60]). Unwanted residues were deleted and the complex was subjected to the default “Structure preparation” module settings. The ‘Site Finder’ feature of MOE 2019 was then employed as previously reported [63,64] in search for the receptor site in the SARS-CoV-2-CTD binding interface [40,60]. The studied compound 5 was prepared via energy minimization and geometry optimization, then docked into the SARS-CoV-2-CTD binding interface. The lowest binding energy conformers with RMSD < 2 Å were inspected compared to hesperidin as a reference being a known viral entry blocker that can lie on the middle shallow pit of the receptor-binding domain (RBD) of spike protein in the interface between spike protein and hACE2 [43]. Docking results revealed that the hit oxadiazole 5 could accommodate into the SARS-CoV-2-CTD binding interface with acceptable free binding energy ($\Delta G = -5.83$ kcal/mol) compared to the reference spike RBD inhibitor hesperidin ($\Delta G = -8.54$ kcal/mol). The best selected binding pose (Fig. 5) showed that our hit compound shared reference-like interactions with some of the key residues involved in the viral RBD-hACE2 complex formation. Therefore, the studied compound may destabilize or even prevent the virus–receptor engagement that is generally dominated by polar contacts mediated by these key hydrophilic amino acid residues [40]. As illustrated (Fig. 5), the oxadiazole core of 5 accepted two H-bonds from the viral RBD Gln493 and Gly496, as well as Lys353 on the hACE2 side. The latter residue also displayed additional cation- π interaction with the heterocyclic core. With that the amino group of the anilino moiety was oriented in the vicinity of the hACE2 His34 residue.

3.4. Structure-activity relationship

The preliminary cytotoxicity screening activity pattern revealed that the studied oxadiazole scaffold (Fig. 2) tolerated different polar groups and conserved their intrinsic safety profiles on normal cells based on previous reports demonstrating their efficient antioxidant activities via different mechanisms [65]. The safety profile of the scaffold was found to be a function of the 2, and 5 positions substitution pattern. The oxadiazol-5-yl aniline derivative 6 with 3-phenyl substituted oxadiazole core displayed the highest safety profile against Wi-38 cells. On the other hand, switching the substitution pattern of 6 led to the positional isomer 10 with nearly one-fold decrease in the safety potential. Further substitution of the oxadiazol-3-yl aniline with pyridin-4-yl (compound 5), or aniline (compound 7) moieties at position 5 of the heterocyclic core allowed supplemental increase in the safety profile. Insertion of phenolic hydroxyl group to the 5-phenyl group of 10 led to slight decrease in the safety of the scaffold. However, further derivatization of amino groups of 10 and its phenolic analogue 4 to the corresponding Schiff's bases 14 and 13, respectively, utilizing mono sodium salt of pyridoxal 5-phosphate led to considerable loss of the compounds' safety relative to their precursors. Formylation of the amino group of 4 (compound 17) enhanced its the safety profile, whereas its acetylation

Table 2Inhibitory activities of the oxadiazole derivatives **4–19** against SARS-CoV-2 Papain-like proteinase (PL pro).

Compound No.	Structure	% Inhibition of PL pro at 10 μ M	IC ₅₀ (μ M)
4		13.6 \pm 1.767	–
5		58.6 \pm 4.030	7.197
6		21.1 \pm 2.616	–
7		16.2 \pm 1.272	–
8		11.7 \pm 1.060	–
9		5.0 \pm 0.424	–
10		20.8 \pm 2.121	–
13		13.9 \pm 1.131	–
14		22.5 \pm 0.565	–
15		17.1 \pm 0.282	–
16		1.1 \pm 0.282	–
17		35.1 \pm 4.596	–

Table 2 (continued)

Compound No.	Structure	% Inhibition of PL pro at 10 μ M	IC ₅₀ (μ M)
18		18.1 \pm 2.404	–
19		5.9 \pm 0.353	–
GRL 0617	–	–	2.05 \pm 0.12 [49]

All values are expressed as mean \pm SEM.

was detrimental to the scaffold's safety profile. Surprisingly, alkylation of **4** and cyclization to the free ester **18** or its carboxylic acid analogue **19** didn't considerably affect its safety. The 2,2'-(1,2,4-oxadiazole-3,5-diyl) diphenol was relatively of moderate safety, whereas the phenolic oxadiazolyl derivative bearing trifluoromethylphenyl substituent **9** didn't show acceptable safety. Considering the safety profile against LT-A549, the highest EC₁₀₀ was recorded for *N*-[2-(5-(2-hydroxyphenyl)-1,2,4-oxadiazol-3-yl) phenyl] formamide (**17**), followed by the dianiline derivative **7**, the oxadiazol-5-yl aniline derivative **6**, and the oxadiazol-3-yl aniline bearing pyridin-4-yl (compound **5**). Other derivatives exhibited low safety profiles except for the 2-(3-phenyl oxadiazol-5-yl) aniline **10**, and the cyclic ester **18** which were considered moderately safe. Further mechanistic anti-corona activities revealed that highest potency against SARS-CoV-2 PLpro was achieved by substitution of the oxadiazol-3-yl aniline with pyridin-4-yl moiety at position 5 of the heterocyclic core (compound **5**), followed by the formamide derivative **17**, the Schiff's base **14** and its oxadiazol-3-yl aniline precursor **10**. Switching the substitution pattern of **10** conferred comparable inhibitory activities as observed by its positional isomer **6**. Other diversification strategies didn't afford acceptable potencies. As for studying the possible viral entry blockade potential of the investigated oxadiazoles, again the 2-[5-(pyridin-4-yl)-1,2,4-oxadiazol-3-yl]aniline (**5**) was the most potent spike protein RBD inhibitor among the series. Accordingly, the best balanced dual inhibitory profiles against SARS-CoV-2 PLpro and spike protein RBD was achieved by substitution of the oxadiazole core with aniline and pyridin-4-yl moieties at positions 3 and 5, respectively (compound **5**). Substitution of the pyridinyl moiety in compound **5** by phenyl (compound **10**), *o*-aminophenyl (compound **7**) or *o*-hydroxyphenyl group (compound **4**) decreased the RBD inhibitory activity by 2.5–3 folds. Switching the heterocyclic core substitution pattern in compound **10** affording its positional isomer; 2-(3-Phenyl-1,2,4-oxadiazol-5-yl) aniline **6** slightly enhanced the RBD inhibitory activity of the scaffold. Transformation of free amine derivatives **4** and **10** to the corresponding Schiff's bases **13** and **14** also allowed supplemental increase in the RBD inhibitory potential. Moreover, formylation of the free amine derivative **4** and full acetylation afforded the equipotent formamide and acetylated derivatives and enhanced the precursor **4** potency by more than 2 folds. On the other hand, the cyclized ester **18** and acid **19** were less active than **4** by nearly 1.2 and 1.8 folds, respectively. 3,5-Disubstitution of the heterocyclic core with two *o*-hydroxyphenyl groups (compound **8**), *p*-trifluoromethylphenyl and *o*-aminophenyl groups (compound **9**) or *o*-azidophenyl and *o*-hydroxyphenyl groups (compound **16**) was detrimental to RBD inhibitory potential.

4. Conclusion

A series of 2,5-diaryl-1,2,4-oxadiazoles were synthesized and

Table 3

Inhibitory activities of the oxadiazole derivatives 4–19 against SARS-CoV-2 spike receptor binding domain (RBD).

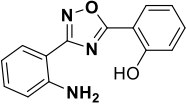
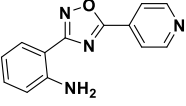
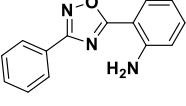
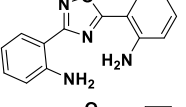
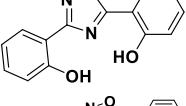
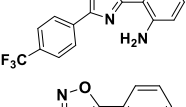
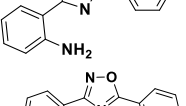
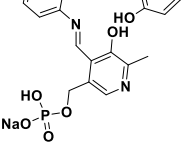
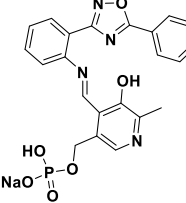
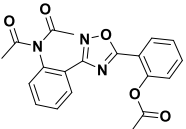
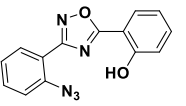
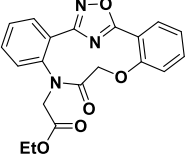
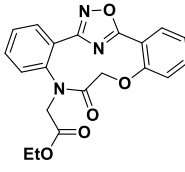
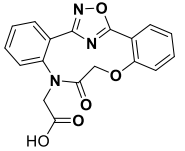
Compound No.	Structure	% Inhibition of spike RBD at 10 μ M	IC ₅₀ (μ M)
4		18.1 \pm 9.820	–
5		65.6 \pm 6.285	8.673
6		31.4 \pm 5.106	–
7		26.1 \pm 5.499	–
8		–50.6 \pm 14.927	–
9		–98.1 \pm 18.463	–
10		23.3 \pm 9.428	–
13		26.1 \pm 5.499	–
14		36.7 \pm 4.714	–
15		44.4 \pm 7.856	–
16		–1617.5 \pm 116.672	–
17		44.3 \pm 7.70	–

Table 3 (continued)

Compound No.	Structure	% Inhibition of spike RBD at 10 μ M	IC ₅₀ (μ M)
18		15.6 \pm 6.285	–
19		10.6 \pm 0.777	–

All values are expressed as mean \pm SEM.

evaluated for their inhibitory potential against SARS-CoV-2 PLpro and spike protein RBD. The design strategy utilized benzamide PLpro inhibitor GRL0617 as a lead compound while replacing its amide backbone by the non-classical isostere 1,2,4-oxadiazole. The substitution pattern at the 2 and 5 positions of the heterocyclic core was rationalized to tune the scaffold's potency against the specified viral targets. The 2-[5-(pyridin-4-yl)-1,2,4-oxadiazol-3-yl] aniline (**5**) was the most potent and balanced dual inhibitor of SARS-CoV-2 PLpro (IC₅₀ = 7.197 μ M) and spike protein RBD (IC₅₀ = 8.673 μ M). It displayed the most promising safety profile, among the series, on both Wi-38 (CC₅₀ = 51.78 μ M) and LT-A549 (CC₅₀ = 45.77 μ M) lung cell lines. The compound obeyed the Lipinski's LogP parameter practically (LogP = 3.8) and demonstrated acceptable ligand efficiency metrics. Docking simulations declared the possible contribution of the oxadiazole core to the scaffold's interaction with the receptor key amino acid residues and enriched the SAR data for further optimization studies. It is worth mentioning that the 2-[5-(pyridin-4-yl)-1,2,4-oxadiazol-3-yl] aniline (**5**) represents a good starting point for further optimization studies. The preliminary viral entry blockade studies should be followed by the resolved cryoEM structure of the promising oxadiazole complexed with RBD in future studies for justification of the mechanism together with enriching the structural basis of inhibition to aid further optimization studies.

5. Experimental

5.1. Chemistry

5.1.1. Materials and equipment

The materials and equipment were reported in the supplementary data.

5.1.2. General method for synthesis amidoximes (2a–d)

A mixture of hydroxylamine hydrochloride (0.015 mol), and sodium bicarbonate (0.015 mol) in absolute EtOH (50.0 ml), were refluxed with stirring for 15 min, then the aromatic nitrile (0.016 mol) namely *o*-hydroxybenzonitrile, *o*-aminobenzonitrile, benzonitrile, or *p*-trifluoromethyl benzonitrile **1a–d** respectively, was added to the mixture and kept stirring with refluxing for 8 h. The resulting mixture was filtered, then evaporated under reduced pressure to afford the corresponding amidoxime **2a–d** that was used directly without purification.

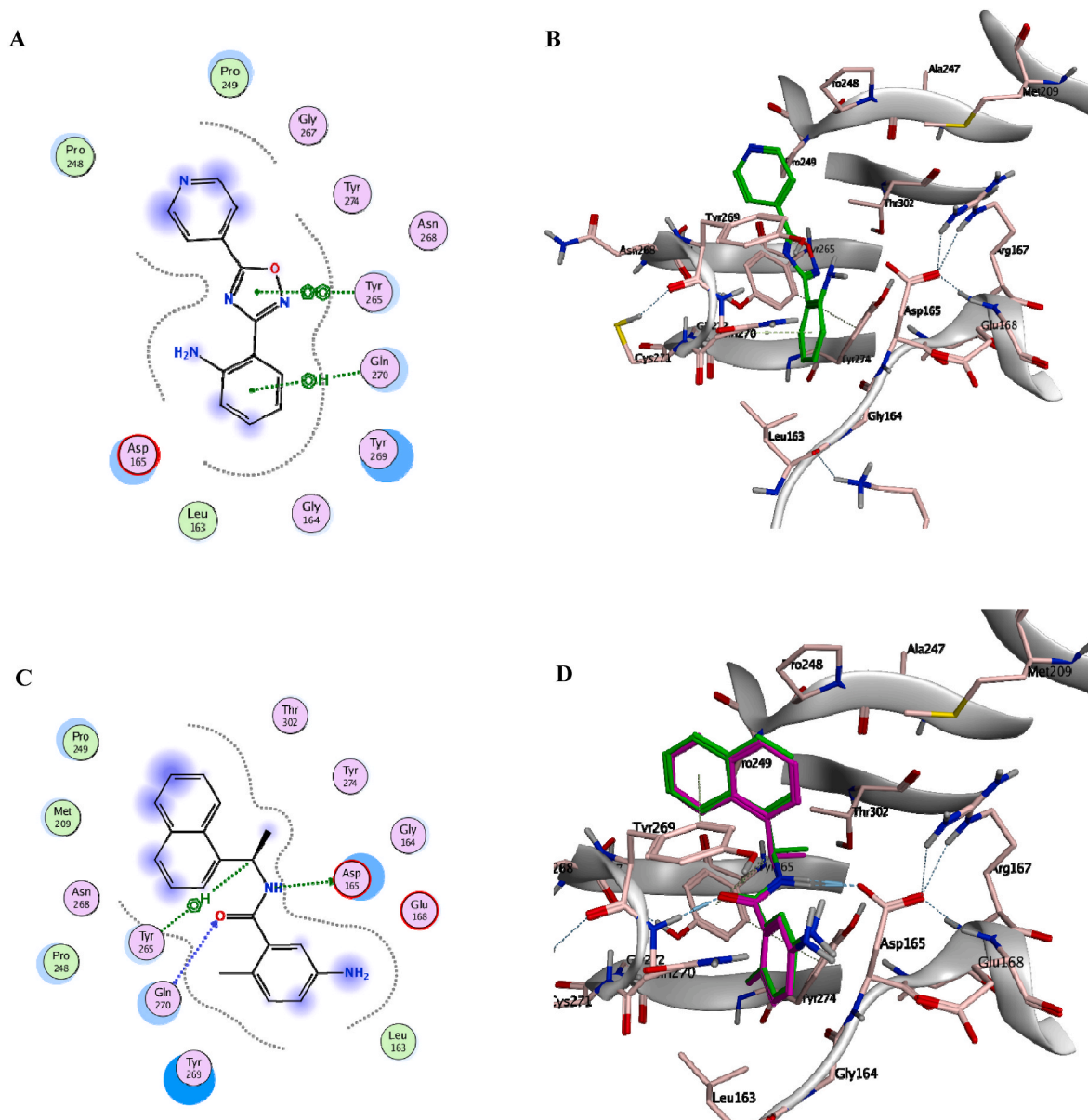
5.1.3. 2 (3-(2-aminophenyl)-1,2,4-oxadiazol-5-yl) phenol (**4**)

A mixture of **2b** (4.0 gm, 0.0169 mol), ethyl salicylate **3a** (4 gm, 0.024 mol) and NaOH (1.6 gm, 0.04 mol) in DMSO (20.0 ml) were stirred for 24 h. The reaction mixture was poured on cold water (0.5 L) with stirring then the mixture was acidified with HCl (2 M). The formed precipitate was filtered, to give **4** as off-white powder (4.6 gm, yield 85%); R_f = 0.6 (EtOAc: n-hexane, 1:1); m.p = 179–181 °C, IR: ν_{\max} /

Table 4

Experimental octanol/water partition coefficient (LogP) and Ligand efficiency metrics of the hit oxadiazole derivative 5.

Compound No.	LogP ^a	NHA ^b	RBD					PLpro				
			IC ₅₀	pIC ₅₀ ^c	LE ^d	LLE ^e	LLEP ^f	IC ₅₀	pIC ₅₀	LE	LLE	LLEP
5	3.8	18	8.673	5.061	0.385	1.261	9.870	7.197	5.142	0.391	1.342	9.718

^a LogP: logarithm of compound's partition coefficient between n-octanol and water.^b NHA = non-hydrogen atom.^c pIC₅₀: half-maximal inhibitory concentration (in term of molar concentration). pIC₅₀ = -log (IC₅₀).^d LE: ligand efficiency. LE = 1.37 (pIC₅₀)/NHA. The lower acceptable limit of LE is 0.3 [53–55].^e LLE: lipophilic ligand efficiency. LLE = pIC₅₀–LogP. LLE values ≥ 3 are acceptable for lead compound, while values ≥ 5 are recommended for drug-like candidate [55,56,59].^f LLEP: ligand efficiency-dependent lipophilicity index = LogP/LE. Optimal values are -10 < LLEP < 10.**Fig. 4.** A) 2D interactions, and B) 3D binding mode of the lowest energy conformer of the oxadiazole derivative 5 (green sticks) with PLpro (PDB ID: 3E9S [26]), C) 2D binding mode, and D) Superposition of the modeled (magenta sticks) and the co-crystallized inhibitor (green sticks), in its binding site.

cm⁻¹ 3400 (OH), 3197, 3073 (NH₂); ¹H NMR (500 MHz, DMSO-*d*₆) δ_H: 10.60 (s, 1H, OH), 7.98 (d, *J* = 8 Hz, 1H, Ar-H), 7.94 (d, *J* = 6.5 Hz, 1H, Ar-H), 7.49 (t, *J* = 6.5 Hz, 1H, Ar-H), 7.21 (t, *J* = 8.0 Hz, 1H, Ar-H), 7.10 (d, *J* = 8.0 Hz, 1H, Ar-H), 7.01 (t, *J* = 8.0 Hz, 2H, Ar-H) 6.85 (d, *J* = 8.0

Hz, 1H, Ar-H), 6.66 (t, *J* = 8.0 Hz, 1H, Ar-H), 6.32 (s, 2H, NH₂); ¹³C NMR (125 MHz, DMSO-*d*₆) δ_C: 173.0, 167.4, 157.3, 147.7, 134.8, 132.1, 130.2, 129.5, 119.8, 117.4, 116.0, 115.6, 109.7, 107.3.

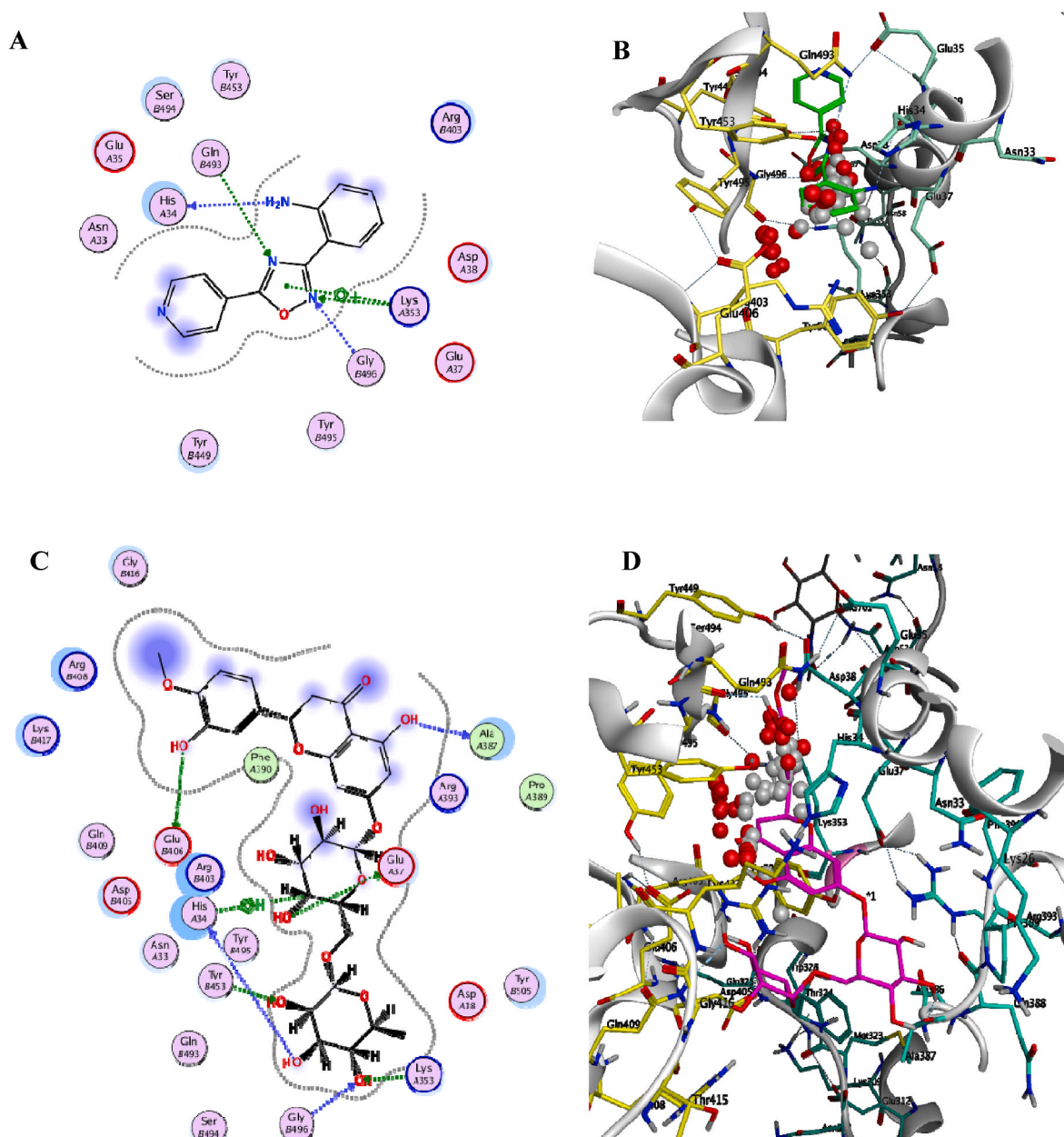


Fig. 5. A) 2D interactions, and B) 3D binding mode of the lowest energy conformer of the oxadiazole derivative **5** (green sticks) into the SARS-CoV-2-CTD binding interface (PDB ID: 6LZG [60]), C) 2D interactions, and D) 3D binding mode of the lowest energy conformer of the hesperidin (magenta sticks) into the SARS-CoV-2-CTD binding interface.

5.1.4. 2-[5-(Pyridin-4-yl)-1,2,4-oxadiazol-3-yl]aniline (**5**)

A mixture of **2b** (100 mg, 0.66 mmol), ethyl isonicotinate **3d** (150 mg, 0.99 mmol) and NaOH (52 mg, 1.32 mmol) in DMSO (5.0 ml), was stirred for 24 h. The reaction mixture was poured onto cold water (30 ml). The formed solid product was filtered then dried to give **5** as yellowish white powder (137.7 mg, yield 80%); $R_f = 0.13$ (DCM: n-hexane, 1:1); m.p = 172–174 °C; IR: $\nu_{\max}/\text{cm}^{-1}$ 3368, 3266 (NH₂); ¹H NMR (500 MHz, DMSO-*d*₆) δ_H : 8.90 (s, 2H, Ar-H), 8.12 (d, $J = 5.0$ Hz, 2H, Ar-H), 7.98 (d, $J = 8.0$ Hz, 1H, Ar-H), 7.26 (t, $J = 7.5$ Hz, 1H, Ar-H), 6.90 (d, $J = 8.0$ Hz, 1H, Ar-H), 6.71 (t, $J = 8.0$, 1H, Ar-H), 6.37 (s, 2H, NH₂); ¹³C NMR (125 MHz, DMSO-*d*₆) δ_C : 173.5, 168.4, 147.7, 133.4, 132.2, 129.6, 129.4, 128.1, 123.3, 116.0, 115.6, 107.3.

5.1.5. 2-(3-Phenyl-1,2,4-oxadiazol-5-yl) aniline (**6**)

A mixture of amido oxime **2c** (100 mg, 0.73 mmol), ethyl anthranilate **3b** (100 mg, 0.65 mmol) and NaOH (39 mg, 0.97 mmol) in DMSO

(5.0 ml) was stirred for 24 h. The reaction mixture was poured on cold water (20.0 ml). The product was filtered off then dried to give **6** as off-white powder (70 mg, 77% yield); $R_f = 0.68$ (DCM: n-hexane, 1:1); m.p = 94–96 °C; IR: $\nu_{\max}/\text{cm}^{-1}$ 3330, 3068 (NH₂); ¹H NMR (500 MHz, DMSO-*d*₆) δ_H : 8.10 (d, $J = 7.5$ Hz, 2H, Ar-H), 7.80 (d, $J = 7.5$ Hz, 1H, Ar-H), 7.59–7.53 (m, 3H, Ar-H), 7.31 (t, 1H, $J = 7.0$ Hz, Ar-H), 6.96 (s, 2H, NH₂), 6.91 (d, $J = 8.0$ Hz, 1H, Ar-H), 6.65 (t, 1H, $J = 7.5$ Hz, Ar-H); ¹³C NMR (125 MHz, DMSO-*d*₆) δ_C : 175.2, 167.8, 149.4, 134.6, 132.2, 129.8, 129.0, 127.8, 126.7, 117.1, 116.2, 104.0.

5.1.6. 2,2'-(1,2,4-oxadiazole-3,5-diyl) di aniline (**7**)

A mixture of compound **2b** (100 mg, 0.66 mmol), ethyl anthranilate **3b** (100 mg, 0.65 mmol) and NaOH (39 mg, 0.97 mmol) in DMSO (5.0 ml) was stirred for 24 h. The reaction mixture was poured on cold water (20.0 ml). The product was filtered and separated out then dried to give **7** as off-white powder (64 mg, 88% yield); $R_f = 0.46$ (DCM: n-hexane,

1:1); m.p = 138–140 °C; IR: $\nu_{\max}/\text{cm}^{-1}$ 3306, 3190 (NH₂); ¹H NMR (500 MHz, DMSO-*d*₆) δ_{H} : 8.02 (d, *J* = 8.0 Hz, 1H, Ar -H), 7.81 (d, *J* = 8.0 Hz, 1H, Ar-H), 7.31 (t, *J* = 7.5 Hz, 1H, Ar-H), 7.23 (t, *J* = 7.5 Hz, 1H, Ar -H), 6.95–6.92 (m, 3H, Ar -H), 6.85 (d, *J* = 8.0 Hz, 1H, Ar -H), 6.66 (q, *J* = 15.5, 8.0 Hz, 2H, NH₂), 6.31 (s, 2H, NH₂); ¹³C NMR (125 MHz, DMSO-*d*₆) δ_{C} : 173.2, 168.0, 149.4, 148.1, 134.6, 132.5, 130.3, 129.1, 117.1, 116.3, 116.2, 108.0, 103.9.

5.1.7. 2,2'-(1,2,4-oxadiazole-3,5-diyl) diphenol (8)

A mixture of **2a** (2.0 gm, 0.013 mmol), ethyl salicylate (2.0 gm, 0.009 mmol) and NaOH (1.2 gm, 0.03 mmol) in DMSO (20.0 ml) stirred for 24 h. The reaction mixture was poured on cold water (50.0 ml) and acidified with HCl (2 M). The precipitate was filtered off then dried to give **8** as white powder (20 mg, 57% yield); *R*_f = 0.69 (DCM: n-hexane, 1:1); m.p = 159–161 °C; IR: $\nu_{\max}/\text{cm}^{-1}$ 3333 (OH); ¹H NMR (500 MHz, DMSO-*d*₆) δ_{H} : 10.71 (s, 1H, OH), 10.16 (s, 1H, OH), 7.97 (d, *J* = 8.0 Hz, 1H, Ar-H), 7.86 (d, *J* = 8.0 Hz, 1H, Ar -H), 7.51 (t, *J* = 8.5 Hz, 1H, Ar -H), 7.39 (t, *J* = 8.0 Hz, 1H, Ar -H), 7.10 (d, *J* = 8.5 Hz, 1H, Ar -H), 7.03–6.95 (m, 3H, Ar-H).

5.1.8. 2-[3-(4-(Trifluoromethyl) phenyl)-1,2,4-oxadiazol-5-yl] aniline (9)

A mixture of the amido oxime **2d** (100 mg, 0.48 mmol), (100 mg, 0.65 mmol) ethyl anthranilate **3b** and NaOH (39 mg, 0.97 mmol) in DMSO (5.0 ml) was stirred for 24 h. The reaction mixture was poured on cold water (20.0 ml) then filtrated and the product separated out to give **9** as off-white powder (35 mg, 67% yield); *R*_f = 0.53 (DCM: n-hexane, 1:1); m.p = 117–119 °C; IR: $\nu_{\max}/\text{cm}^{-1}$ 3330, 3199 (NH₂); ¹H NMR (500 MHz, DMSO-*d*₆) δ_{H} : 8.32 (d, *J* = 8.0 Hz, 2H, Ar-H), 7.92 (d, *J* = 8.5 Hz, 2H, Ar-H), 7.08 (d, *J* = 8.0 Hz, 1H, Ar-H), 7.31 (t, *J* = 7.0 Hz, 1H, Ar -H), 6.98 (s, 2H, NH₂), 6.93 (d, *J* = 8.5 Hz, 1H, Ar -H), 6.65 (t, *J* = 8.0 Hz, 1H, Ar -H); ¹³C NMR (125 MHz, DMSO-*d*₆) δ_{C} : 175.6, 166.9, 149.5, 134.8, 132.0, 131.8, 130.6, 129.0, 128.6, 126.7, 117.2, 116.2, 103.7.

5.1.9. 2-(3-Phenyl-1,2,4-oxadiazol-5-yl) aniline (10)

A mixture of **2b** (100 mg, 0.66 mmol), benzyl benzoate **3c** (209.8 mg, 1.0 mmol) and NaOH (52.8 mg, 1.32 mmol) in DMSO (3.0 ml) was stirred for 24 h. The reaction mixture was poured on cold water (30.0 ml). The desired product was filtered off then dried to give **10** as white powder (130 mg, 82% yield); *R*_f = 0.56 (DCM: n-hexane, 1:1); m.p = 95–97 °C; IR: $\nu_{\max}/\text{cm}^{-1}$ 3462, 3368 (NH₂); ¹H NMR (500 MHz, DMSO-*d*₆) δ_{H} : 8.20 (d, *J* = 8.0 Hz, 2H, Ar -H), 7.98 (d, *J* = 7.5 Hz, 1H, Ar-H), 7.73 (t, *J* = 7.0 Hz, 1H, Ar-H), 7.65 (t, *J* = 7.5 Hz, 2H, Ar -H), 7.26 (t, *J* = 8.0 Hz, 1H, Ar -H), 6.88 (d, *J* = 8.0 Hz, 1H, Ar -H), 6.70 (t, *J* = 7.0 Hz, 1H, Ar -H), 6.36 (s, 2H, NH₂); ¹³C NMR (125 MHz, DMSO-*d*₆) δ_{C} : 172.0, 168.7, 151.2, 147.8, 132.4, 130.4, 129.4, 121.5 (2C), 116.1, 115.7, 106.9.

5.1.10. Sodium (E)-(6-hydroxy-4-((2-(5-(2-hydroxyphenyl)-1,2,4-oxadiazol-3-yl) phenyl) imino) methyl)-5-methylpyridin-3-yl) methyl hydrogen phosphate (13)

A solution of compound **4** (50 mg, 0.19 mmol) and monosodium salt of pyridoxal of 5-phosphate (71.7 mg, 0.22 mmol) in absolute ethanol (10.0 ml) was refluxed for 3 h, then left to cool at room temperature. The solid product was filtrated off then dried to give **13** as white crystals (70 mg, yield 80%); m.p = 206–208 °C; IR: $\nu_{\max}/\text{cm}^{-1}$ 3440 (OH), 1600 (C=N); ¹H NMR (500 MHz, DMSO-*d*₆) δ_{H} : 13.25 (s, 1H, Acidic-OH), 9.36 (s, 2H, 2OH), 8.06 (s, 2H, Ar-H), 7.93 (d, 1H, *J* = 8.0 Hz, Ar -H), 7.89 (d, *J* = 8.0 Hz, 1H, Ar -H), 7.80–7.73 (m, 2H, Ar -H), 7.52–7.45 (m, 2H, Ar -H), 6.91–6.86 (m, 1H, Ar -H), 5.17 (d, *J* = 7.5 Hz, 2H, CH₂), 2.42 (s, 3H, CH₃); ¹³C NMR (125 MHz, DMSO-*d*₆) δ_{C} : 171.9, 161.2, 151.6, 135.6, 134.7, 133.9, 133.4, 132.4, 130.3, 128.7, 119.6, 119.1, 118.2, 117.1, 115.8, 115.2, 113.1, 108.6, 93.3, 62.0, 19.0.

5.1.11. Sodium-[6-hydroxy-5-methyl-4-((2-(5-phenyl-1,2,4-oxadiazol-3-yl) phenyl) imino) methyl] pyridin-3-yl) methyl hydrogen phosphate (14)

To a solution of compound **10** (50 mg, 0.266 mmol), mono sodium

salt of pyridoxal of 5-phosphate (71.7 mg, 0.22 mmol) in absolute ethanol (15.0 ml) was added. The reaction mixture was refluxed for 3 h, then left to cool. The solid was filtrated and dried to give **14** as off white powder (70 mg, yield 80%); m.p = 199–201 °C; IR: $\nu_{\max}/\text{cm}^{-1}$ 3440 (OH), 1600 (CN); ¹H NMR (500 MHz, DMSO-*d*₆) δ_{H} : 13.38 (s, 1H, Acidic-H), 9.49 (s, 1H, OH), 8.25 (d, *J* = 8.0 Hz, 2H, Ar-H), 8.09 (d, *J* = 8.0 Hz, 1H, Ar-H), 7.95 (d, *J* = 8.0 Hz, 1H, Ar -H), 7.88 (s, 1H, Ar -H), 7.72 (t, *J* = 8.0 Hz, 1H, Ar -H), 7.64 (t, *J* = 7.0 Hz, 3H, Ar -H), 7.48 (t, *J* = 7.0 Hz, 1H, N=C-H), 4.87 (d, *J* = 5.0 Hz, 2H, CH₂), 2.39 (s, 3H, CH₃).

5.1.12. 2-(3-(2-(N-acetylacetamido) phenyl)-1,2,4-oxadiazol-5-yl) phenyl acetate (15)

A solution of compound **4** (100 mg, 0.42 mmol) in acetic anhydride (5.0 ml) was refluxed for 4 h. The reaction mixture was poured onto crushed ice. The product was filtered off and recrystallized from ethanol to give **15** as colorless crystals (96 mg, 84% yield); *R*_f = 0.13 (DCM: n-hexane, 1:1); m.p = 147–149 °C; IR: $\nu_{\max}/\text{cm}^{-1}$ 1721, 1735 (Ac); ¹H NMR (500 MHz, DMSO-*d*₆) δ_{H} : 8.26–8.15 (m, 2H, Ar-H), 7.79–7.65 (m, 3H, Ar-H), 7.59–7.51 (m, 2H, Ar-H), 7.43–7.39 (m, 1H, Ar-H), 2.37 (s, 3H, OAc), 2.14 (s, 6H, 2 N-Ac); ¹³C NMR (125 MHz, DMSO-*d*₆) δ_{C} : 172.4, 172.1 (2C), 169.2, 166.4, 148.9, 138.2, 135.0, 132.8, 131.3, 130.4, 130.2 (2C), 129.7, 127.2, 124.7, 124.6, 116.8, 26.7, 20.9.

5.1.13. 2-[3-(2-Azidophenyl)-1,2,4-oxadiazol-5-yl] phenol (16)

To a solution of compound **4** (238 mg, 1.0 mmol) in glacial acetic acid (10.0 ml) at 0 °C, a cold solution of NaNO₂ (100 mg, 1.44 mmol) in water (1.0 ml) was gradually added followed by a solution of NaN₃ (100 mg, 1.53 mmol) in water (1.0 ml). The mixture was kept at 0–5 °C with stirring for 3 h. The formed precipitate was filtered off and dried to give **15** as a white powder (186 mg, 79% yield); *R*_f = 0.67 (DCM: n-hexane, 1:1); m.p = 103–105 °C; IR: $\nu_{\max}/\text{cm}^{-1}$ 3400 (OH), 2131, 2096 (N₃); ¹H NMR (500 MHz, DMSO-*d*₆) δ_{H} : 10.65 (s, 1H, OH), 7.97 (t, *J* = 8.0 Hz, 2H, Ar-H), 8.02–7.95 (m, 1H, Ar -H), 7.96–7.66 (m, 2H, Ar -H), 7.39 (t, *J* = 8.0 Hz, 1H, Ar -H), 7.12 (d, *J* = 8.0 Hz, 1H, Ar -H), 7.04 (t, *J* = 8.0 Hz, 1H, Ar-H); ¹³C NMR (125 MHz, DMSO-*d*₆) δ_{C} : 174.3, 165.4, 157.2, 138.3, 134.8, 132.6, 131.2, 130.1, 125.3, 120.4, 119.8, 117.8, 117.4, 109.7.

5.1.14. N-[2-(5-(2-hydroxyphenyl)-1,2,4-oxadiazol-3-yl) phenyl] formamide (17)

A mixture of **4** (100 mg, 0.42 mmol) in formic acid (3.0 ml, 95%) was heated near the boiling point for 2 h, then cooled to room temperature. The formed product was filtered and recrystallized from ethanol to give **17** as colorless crystals (130 mg, 85% yield); *R*_f = 0.30 (DCM: n-hexane, 1:1); m.p = 153–155 °C; IR: $\nu_{\max}/\text{cm}^{-1}$ 3414 (OH), 3313 (NH), 1710 (CHO); ¹H NMR (500 MHz, DMSO-*d*₆) δ_{H} : 10.72 (s, 1H, OH), 10.17 (s, 1H, NH), 8.47 (s, 1H, HC=O), 8.34 (d, *J* = 8.0 Hz, 1H, Ar -H), 8.05 (d, *J* = 8.0 Hz, 2H, Ar -H), 7.60–7.53 (m, 2H, Ar-H), 7.33 (t, *J* = 8.0 Hz, 1H, Ar -H), 7.12 (d, *J* = 8.0 Hz, 1H, Ar -H), 7.05 (t, *J* = 8.0 Hz, 1H, Ar-H); ¹³C NMR (125 MHz, DMSO-*d*₆) δ_{C} : 174.5, 166.3, 160.7, 157.4, 136.3, 135.0, 132.0, 130.5, 129.8, 124.5, 122.4, 119.8, 117.5, 115.8, 109.7.

5.1.15. Ethyl (Z)-2-(7-oxo-6,7-dihydro-8H-13,16-(azeno)dibenzo[d,j][1,9]dioxo[2,6]diazacyclodecin-8-yl)acetate (18)

A mixture of compound **4** (100 mg, 0.395 mmol), ethyl bromoacetate (100 mg, 0.598 mmol) and potassium carbonate (100 mg, 0.724 mmol) in DMF (20.0 ml) was refluxed for 24 h. The reaction mixture was poured on cold water (20.0 ml) stirred then separated out to give **18** as yellow powder (25 mg, yield 61%); *R*_f = 0.28 (DCM: n-hexane, 1:1); m.p = 169–171 °C; IR: $\nu_{\max}/\text{cm}^{-1}$ 1768 (C=O), 1650 (OCN); ¹H NMR (500 MHz, DMSO-*d*₆) δ_{H} : 8.27–6.81 (m, 8H, Ar -H), 5.71 (s, 2H, CH₂), 4.16–3.85 (dd, *J* = 8.0 Hz, 4H, CH₂), 1.2 (s, 3H, CH₃); ¹³C NMR (125 MHz, DMSO-*d*₆) δ_{C} : 196.0, 175.0, 174.6, 174.5, 142.0, 141.6, 141.5, 138.0, 137.6, 137.4, 133.3, 132.3, 130.1, 129.4, 129.1, 129.0, 56.2, 52.9, 45.0, 19.3.

5.1.16. (Z)-2-(7-oxo-6,7-dihydro-8H-13,16-(azeno)dibenzo[d,j][1,9]dioxo[2,6]diazacyclododecin-8-yl)acetic acid (19)

A mixture of compound **18** (100 mg, 0.26 mmol), and NaOH (100 mg, 2.5 mmol) in a mixture of dioxane/water (10 ml. 1:1) was refluxed for 3 h, then cooled and acidified to pH = 2 using conc. HCl. The formed product was filtered, then purified by flash column chromatography to give **19** as yellowish powder (33 mg, 63% yield); R_f = 0.06 (DCM: n-hexane, 1:1); m.p = 190–192 °C; IR: $\nu_{\max}/\text{cm}^{-1}$ 3453(OH), 1788(C=O), 1688 (O=CN). ^1H NMR (500 MHz, DMSO- d_6) δ H: 13.03 (bs, 1H, OH), 8.07 (dd, J = 8.0 Hz, 2H, Ar-H), 7.62 (t, J = 7.5 Hz, 1H, Ar-H), 7.36 (t, J = 7.5 Hz, 1H, Ar-H), 7.23–7.17 (m, 2H, Ar -H), 6.76 (t, J = 7.5 Hz, 1H, Ar -H), 6.71 (d, J = 8.0 Hz, 1H, Ar -H), 4.94 (s, 2H, CH₂), 4.06 (s, 2H, CH₂); ^{13}C NMR (125 MHz, DMSO- d_6) δ C: 173.7, 172.4, 170.3, 168.0, 157.4, 146.6, 135.2, 133.1, 132.0, 130.2, 121.9, 116.4, 114.3, 113.0, 112.1, 109.0, 65.6, 45.3.

5.2. Biology

5.2.1. Cytotoxicity screening of the tested compounds against lung cell lines

Normal human lung fibroblast (Wi-38) and long-term cultivated human lung cancer (LT-A549) cell lines were used to detect cytotoxicity of the studied compounds. The latter cell line was utilized as model for alveolar epithelial type II (ATII) which is the main target cell of SARS2-CoV-2. LT-A549, upon its cultivation in Ham's F12 medium for a long term (25 days), represents a more suitable source of functional ATII cells [66]. MTT assay was performed as previously mentioned [67] and detailed in the supplementary data.

5.2.2. Papain-like proteinase (PLpro) inhibition assay

Papain-like proteinase (PLpro) 40 μl volume of 142 nM PLpro in bufer A [50 mM HEPES, pH 7.5; 0.1 mg/ml bovine serum albumin (BSA), and 5 mM Dithiothreitol (DTT)] was dispensed in 96 well plat and then incubated with 100 μl of different concentrations of the tested compounds for 5 min. Reactions were initiated by the addition of a fluorogenic substrate, Arg-Leu-Arg-Gly-Gly-AMC (Enzo Biochem, USA) (RLRGAMC, 10 μl of 250 μM) in buffer A, shaken vigorously for 30 s, and then incubated for 6 min. The reactions were subsequently quenched with 10 μl acetic acid (0.5 M), shaken for 30 s, and measured for fluorescence emission intensity (excitation λ : 360 nm; emission λ : 460 nm). Finally, percentage of inhibition (%) was detected.

5.2.3. Spike protein receptor binding domain (RBD) inhibition assay

Firstly SARS-CoV-2, RBD (1 $\mu\text{g}/\text{ml}$) was incubated with the tested compounds at 37 °C for 2 h then in these proteins was added in well plate overnight at 4 °C and blocked with 2% fat-free milk in PBST for 2 h at 37 °C. 100 μl of sACE2protein was added to the plates and incubated for 2 h at 37 °C. After four washes, the bound protein was detected using hACE2-specific goat antibody (0.5 $\mu\text{g}/\text{ml}$, R&D system) for 2 h at 37 °C, followed by incubation with HRP conjugated anti-goat IgG antibody (1:5,000, Thermo Fisher Scientific) for 1 h at 37 °C. The reaction was visualized by addition of substrate 3,3',5,5'-Tetramethylbenzidine (TMB) (Sigma, St. Louis, MO) and stopped by H₂SO₄ (1 N). The absorbance at 450 nm (A450) was measured by an ELISA plate reader (Tecan, San Jose, CA) [68,69].

5.2.4. Octanol/water partition coefficient (LogP) determination

The octanol/water partition coefficient (LogP) was experimentally determined according to the capacity factor calculation method employing RP-HPLC [50,51,70] and detailed in the supplementary data.

5.3. Docking simulations

Docking was conducted employing Molecular Operating Environment (MOE) software package version MOE 2019.102, Chemical Computing Group, Montreal, Canada as detailed in the supplementary data.

5.4. Data analysis and statistics

Statistical analysis is described in the supplementary data.

Declaration of competing interest

The authors declare that they have no known competing financial interests or personal relationships that could have appeared to influence the work reported in this paper.

Data availability

Data will be made available on request.

Acknowledgement

M. S. A. expresses sincere gratitude to Faculty of Science, Alexandria University (Egypt), and Academy of Scientific Research and Technology (ASRT) for funding the project 7207.

Appendix A. Supplementary data

Supplementary data to this article can be found online at <https://doi.org/10.1016/j.ejmech.2023.115272>.

References

- [1] J.H. University, meicine, coronavirus research center. <https://coronavirus.jhu.edu/map.html>. Jun (2022).
- [2] F. Krammer, SARS-CoV-2 vaccines in development, *Nature* 586 (2020) 516–527.
- [3] A.-T. Ton, M. Pandey, J.R. Smith, F. Ban, M. Fernandez, A. Cherkasov, Targeting SARS-CoV-2 papain-like protease in the post-vaccine era, *Trends Pharmacol. Sci.* 43 (2022) 906–919.
- [4] S.O. Aftab, M.Z. Ghouri, M.U. Masood, Z. Haider, Z. Khan, A. Ahmad, N. Munawar, Analysis of SARS-CoV-2 RNA-dependent RNA polymerase as a potential therapeutic drug target using a computational approach, *J. Transl. Med.* 18 (2020) 1–15.
- [5] Z. Jin, X. Du, Y. Xu, Y. Deng, M. Liu, Y. Zhao, B. Zhang, X. Li, L. Zhang, C. Peng, Structure of Mpro from SARS-CoV-2 and discovery of its inhibitors, *Nature* 582 (2020) 289–293.
- [6] W. Dai, B. Zhang, X.-M. Jiang, H. Su, J. Li, Y. Zhao, X. Xie, Z. Jin, J. Peng, F. Liu, Structure-based design of antiviral drug candidates targeting the SARS-CoV-2 main protease, *Scientometrics* 368 (2020) 1331–1335.
- [7] D.V. Parums, current status of oral antiviral drug treatments for SARS-CoV-2 infection in non-hospitalized patients, *Med. Sci. Mon. Int. Med. J. Exp. Clin. Res.: Int. J. Clin. Exp. Med.* 28 (2022), e935952, 935951.
- [8] T.K. Burki, The role of antiviral treatment in the COVID-19 pandemic, *Lancet Respir. Med.* 10 (2022) e18.
- [9] M. Kozlov, Merck's COVID pill loses its lustre: what that means for the pandemic, *Nature* (2021). <https://www.nature.com/articles/d41586-021-03667-0> (accessed in 1st December 2022).
- [10] J. Heskin, S.J.C. Pallett, N. Mughal, G.W. Davies, L.S.P. Moore, M. Rayment, R. Jones, Caution required with use of ritonavir-boosted PF-07321332 in COVID-19 management, *Lancet* 399 (2022) 21–22.
- [11] M.D. Sacco, Y. Hu, M.V. Gongora, F. Meilleur, M.T. Kemp, X. Zhang, J. Wang, Y. Chen, The P132H mutation in the main protease of Omicron SARS-CoV-2 decreases thermal stability without compromising catalysis or small-molecule drug inhibition, *Cell Res.* 32 (2022) 498–500.
- [12] J.A. Mótyán, M. Mahdi, G. Hoffka, J. Tózsér, Potential resistance of SARS-CoV-2 main protease (Mpro) against protease inhibitors: lessons learned from HIV-1 protease, *Int. J. Mol. Sci.* 23 (2022) 3507.
- [13] S. Iketani, H. Mohri, B. Culbertson, S.J. Hong, Y. Duan, M.I. Luck, M. K. Annavajhala, Y. Guo, Z. Sheng, A.-C. Uhlemann, Multiple pathways for SARS-CoV-2 resistance to nirmatrelvir, *Nature* (2022) 1–3.
- [14] Y. Hu, E.M. Lewandowski, H. Tan, X. Zhang, R.T. Morgan, X. Zhang, L.M.C. Jacobs, S.G. Butler, M.V. Gongora, J. Choy, Naturally Occurring Mutations of SARS-CoV-2 Main Protease Confer Drug Resistance to Nirmatrelvir, *BioRxiv*, 2022, 2022-2006.
- [15] H. Tan, Y. Hu, P. Jadhav, B. Tan, J. Wang, Progress and challenges in targeting the SARS-CoV-2 papain-like protease, *J. Med. Chem.* 65 (2022) 7561–7580.
- [16] S. Ullrich, C. Nitsche, SARS-CoV-2 papain-like protease: structure, function and inhibition, *Chembiochem* 23 (2022), e202200327.
- [17] D.J. Calleja, G. Lessene, D. Komander, Inhibitors of SARS-CoV-2 PLpro, *Front. Chem.* 10 (2022).
- [18] H. Ledford, COVID antiviral pills: what scientists still want to know, *Nature* 599 (2021) 358–359.
- [19] A. Narayanan, M. Narwal, S.A. Majowicz, C. Varricchio, S.A. Toner, C. Ballatore, A. Brancale, K.S. Murakami, J. Jose, Identification of SARS-CoV-2 inhibitors

- targeting Mpro and PLpro using in-cell-protease assay, *Commun. Biol.* 5 (2022) 1–17.
- [20] C.B. McClain, N. Vabret, SARS-CoV-2: the many pros of targeting PLpro, *Signal Transduct. Targeted Ther.* 5 (2020) 1–2.
- [21] D. Shin, R. Mukherjee, D. Grewe, D. Bojkova, K. Baek, A. Bhattacharya, L. Schulz, M. Wiedera, A.R. Mehdipour, G. Tascher, Papain-like protease regulates SARS-CoV-2 viral spread and innate immunity, *Nature* 587 (2020) 657–662.
- [22] W. Li, J. Qiao, Q. You, S. Zong, Q. Peng, Y. Liu, S. Hu, W. Liu, S. Li, X. Shu, SARS-CoV-2 Nsp5 activates NF- κ B pathway by upregulating SUMOylation of MAVS, *Front. Immunol.* 12 (2021).
- [23] D.M. Del Valle, S. Kim-Schulze, H.-H. Huang, N.D. Beckmann, S. Nirenberg, B. Wang, Y. Lavin, T.H. Swartz, D. Madduri, A. Stock, An inflammatory cytokine signature predicts COVID-19 severity and survival, *Nat. Med.* 26 (2020) 1636–1643.
- [24] X. Gao, B. Qin, P. Chen, K. Zhu, P. Hou, J.A. Wojdyla, M. Wang, S. Cui, Crystal structure of SARS-CoV-2 papain-like protease, *Acta Pharm. Sin. B* 11 (2021) 237–245.
- [25] H. Jiang, P. Yang, J. Zhang, Potential inhibitors targeting papain-like protease of SARS-CoV-2: two birds with one stone, *Front. Chem.* 10 (2022).
- [26] D. Shin, R. Mukherjee, D. Grewe, D. Bojkova, K. Baek, A. Bhattacharya, L. Schulz, M. Wiedera, A.R. Mehdipour, G. Tascher, P.P. Geurink, A. Wilhelm, G.J. van der Heden van Noort, H. Ovaa, S. Müller, Klaus-Peter Knobeloch, K. Rajalingam, B. A. Schulman, J. Cinatl, G. Hummer, S. Ciesek, Papain-like protease regulates SARS-CoV-2 viral spread and innate immunity, *Nature* 587 (2020) 657–662.
- [27] Z. Fu, B. Huang, J. Tang, S. Liu, M. Liu, Y. Ye, Z. Liu, Y. Xiong, W. Zhu, D. Cao, The complex structure of GRL0617 and SARS-CoV-2 PLpro reveals a hot spot for antiviral drug discovery, *Nat. Commun.* 12 (2021) 1–12.
- [28] A.-T. Ton, M. Pandey, J.R. Smith, F. Ban, M. Fernandez, A. Cherkasov, Targeting SARS-CoV-2 papain-like protease in the postvaccine era, *Trends Pharmacol. Sci.* 43 (2022) 906–919.
- [29] I. Song, H. Lee, S.W. Jeon, I.A.M. Ibrahim, J. Kim, Y. Byun, D.J. Koh, J.W. Han, D. H. Kim, Simple physical mixing of zeolite prevents sulfur deactivation of vanadia catalysts for NO_x removal, *Nat. Commun.* 12 (2021) 1–9.
- [30] C. Ma, M.D. Sacco, Z. Xia, G. Lambiridis, J.A. Townsend, Y. Hu, X. Meng, T. Szeto, M. Ba, X. Zhang, Discovery of SARS-CoV-2 papain-like protease inhibitors through a combination of high-throughput screening and a FlipGFP-based reporter assay, *ACS Comb. Sci.* 7 (2021) 1245–1260.
- [31] H. Shan, J. Liu, J. Shen, J. Dai, G. Xu, K. Lu, C. Han, Y. Wang, X. Xu, Y. Tong, Development of potent and selective inhibitors targeting the papain-like protease of SARS-CoV-2, *Cell Chem. Biol.* 28 (2021) 855–865.
- [32] T. Klemm, G. Ebert, D.J. Calleja, C.C. Allison, L.W. Richardson, J.P. Bernardini, B. G.C. Lu, N.W. Kuchel, C. Grohmann, Y. Shibata, Z.Y. Gan, J.P. Cooney, M. Doerflinger, A.E. Au, T.R. Blackmore, G.J. van der Heden van Noort, P. P. Geurink, H. Ovaa, J. Newman, A. Riboldi-Tunnicliffe, P.E. Czabotar, J. P. Mitchell, R. Feltham, B.C. Lechtenberg, K.N. Lowes, G. Dewson, M. Pellegrini, G. Lessene, D. Komander, Mechanism and inhibition of the papain-like protease, PLpro, of SARS-CoV-2, *The EMBO J.* 39 (2020), e106275.
- [33] Z. Shen, K. Ratia, L. Cooper, D. Kong, H. Lee, Y. Kwon, Y. Li, S. Alqarni, F. Huang, O. Dubrovskiy, Design of SARS-CoV-2 PLpro inhibitors for COVID-19 antiviral therapy leveraging binding cooperativity, *J. Med. Chem.* 65 (2021) 2940–2955.
- [34] K. Ratia, S. Pegam, J. Takayama, K. Sleeman, M. Coughlin, S. Baliji, R. Chaudhuri, W. Fu, B.S. Prabhakar, M.E. Johnson, S.C. Baker, A.K. Ghosh, A.D. Mesecar, A noncovalent class of papain-like protease/deubiquitinase inhibitors blocks SARS virus replication, *Proc. Natl. Acad. Sci. U.S.A.* 105 (2008) 16119–16124.
- [35] S. Urig, K. Becker, On the potential of thioredoxin reductase inhibitors for cancer therapy, *Semin. Cancer Biol.* 16 (2006) 452–465.
- [36] J. Boström, A. Hogner, A. Llinas, E. Wellner, A.T. Plowright, Oxadiazoles in medicinal chemistry, *J. Med. Chem.* 55 (2012) 1817–1830.
- [37] B.M. Hybertson, B. Gao, S.K. Bose, J.M. McCord, Oxidative stress in health and disease: the therapeutic potential of Nrf2 activation, *Mol. Aspect. Med.* 32 (2011) 234–246.
- [38] W. Dröge, Free radicals in the physiological control of cell function, *Physiol. Rev.* 1 (2002) 47–95.
- [39] X.-Y. Ge, J.-L. Li, X.-L. Yang, A.A. Chmura, G. Zhu, J.H. Epstein, J.K. Mazet, B. Hu, W. Zhang, C. Peng, Isolation and characterization of a bat SARS-like coronavirus that uses the ACE2 receptor, *Nature* 503 (2013) 535–538.
- [40] Q. Wang, Y. Zhang, L. Wu, S. Niu, C. Song, Z. Zhang, G. Lu, C. Qiao, Y. Hu, K.-Y. Yuen, Structural and functional basis of SARS-CoV-2 entry by using human ACE2, *Cell* 181 (2020) 894–904.
- [41] A.O. Adediji, W. Severson, C. Jonsson, K. Singh, S.R. Weiss, S.G. Sarafianos, Novel inhibitors of severe acute respiratory syndrome coronavirus entry that act by three distinct mechanisms, *J. Virol.* 87 (2013) 8017–8028.
- [42] M.J. Vincent, E. Bergeron, S. Benjannet, B.R. Erickson, P.E. Rollin, T.G. Ksiazek, S. C. i, Chloroquine is a potent inhibitor of, spread, *Virol.* Chloroquine is a potent inhibitor of SARS coronavirus infection and spread, *J. J* 2 (2005) 69.
- [43] C. Wu, Y. Liu, Y. Yang, P. Zhang, W. Zhong, Y. Wang, Q. Wang, Y. Xu, M. Li, X. Li, Analysis of therapeutic targets for SARS-CoV-2 and discovery of potential drugs by computational methods, *Acta Pharm. Sin. B* 10 (2020) 766–788.
- [44] F.-J. Cheng, T.-K. Huynh, C.-S. Yang, D.-W. Hu, Y.-C. Shen, C.-Y. Tu, Y.-C. Wu, C.-H. Tang, W.-C. Huang, Y. Chen, Hesperidin is a potential inhibitor against SARS-CoV-2 infection, *Nutrients* 13 (2021) 2800.
- [45] A.V. Afonin, I.A. Ushakov, A.V. Vashchenko, D.E. Simonenko, A.V. Ivanov, A. M. Vasil'tsov, A.b.i. Mikhaleva, B.A. Trofimov, C-H...N and C-H...O intramolecular hydrogen bonding effects in the ¹H, ¹³C and ¹⁵N NMR spectra of the configurational isomers of 1-vinylpyrrole-2-carbaldehyde oxime substantiated by DFT calculations, *Magn. Reson. Chem.* 47 (2009) 105–112.
- [46] M. Carcatera, C. Caruso, Alveolar epithelial cell type II as main target of SARS-CoV-2 virus and COVID-19 development via NF-Kb pathway deregulation: a physio-pathological theory, *Med. Hypotheses* 146 (2021), 110412.
- [47] J.R. Cooper, M.B. Abdullatif, E.C. Burnett, K.E. Kempell, F. Conforti, H. Tolley, J. E. Collins, D.E. Davies, Long term culture of the A549 cancer cell line promotes multilamellar body formation and differentiation towards an alveolar type II pneumocyte phenotype, *PLoS One* 11 (2016), e0164438.
- [48] D.A. Ghareeb, S.R. Saleh, M.G. Seadawy, M.S. Nofal, S.A. Abdulmalek, S.F. Hassan, S.M. Khedr, M.G. Abdelwahab, A.A. Sobhy, A.M. Yassin, Nanoparticles of ZnO/Berberine complex contract COVID-19 and respiratory co-bacterial infection in addition to elimination of hydroxychloroquine toxicity, *J. Pharm. Investig.* 51 (2021) 735–757.
- [49] Z. Fu, B. Huang, J. Tang, S. Liu, M. Liu, Y. Ye, Z. Liu, Y. Xiong, W. Zhu, D. Cao, The complex structure of GRL0617 and SARS-CoV-2 PLpro reveals a hot spot for antiviral drug discovery, *Nat. Commun.* 12 (2021) 488.
- [50] K. Valkó, Application of high-performance liquid chromatography-based measurements of lipophilicity to model biological distribution, *J. Chromatogr. A* 1037 (2004) 299–310.
- [51] Y.-P. Chin, W.J. Weber, T.C. Voice, Determination of partition coefficients and aqueous solubilities by reverse phase chromatography—II: evaluation of partitioning and solubility models, *Water Res.* 20 (1986) 1443–1450.
- [52] C.A. Lipinski, F. Lombardo, B.W. Dominy, P.J. Feeney, Experimental and computational approaches to estimate solubility and permeability in drug discovery and development settings, *Adv. Drug Deliv. Rev.* 23 (1997) 3–25.
- [53] M. Salah Ayoup, Y. Wahby, H. Abdel-Hamid, E.S. Ramadan, M. Teleb, M.M. Abu-Serie, A. Noby, Design, synthesis and biological evaluation of novel α -acyloxy carboxamides via Passerini reaction as caspase 3/7 activators, *Eur. J. Med. Chem.* 168 (2019) 340–356.
- [54] H. Chen, O. Engkvist, T. Kogej, Chapter 15 - compound properties and their influence on drug quality, in: C.G. Wermuth, D. Aldous, P. Raboisson, D. Rognan (Eds.), *The Practice of Medicinal Chemistry*, fourth ed., Academic Press, San Diego, 2015, pp. 379–393.
- [55] G.M. Keseri, G.M. Makara, The influence of lead discovery strategies on the properties of drug candidates, *Nat. Rev. Drug Discov.* 8 (2009) 203–212.
- [56] I. Jabeen, K. Pleban, U. Rinner, P. Chiba, G.F. Ecker, Structure–activity relationships, ligand efficiency, and lipophilic efficiency profiles of benzophenone-type inhibitors of the multidrug transporter P-glycoprotein, *J. Med. Chem.* 55 (2012) 3261–3273.
- [57] T.T. Wager, R.Y. Chandrasekaran, X. Hou, M.D. Troutman, P.R. Verhoest, A. Villalobos, Y. Will, Defining desirable central nervous system drug space through the alignment of molecular properties, in vitro ADME, and safety attributes, *ACS Chem. Neurosci.* 1 (2010) 420–434.
- [58] E.S.H. El Ashry, L.F. Awad, M. Teleb, N.A. Ibrahim, M.M. Abu-Serie, M.N. Abd Al Moaty, Structure-based design and optimization of pyrimidine- and 1,2,4-triazolo [4,3-a]pyrimidine-based matrix metalloproteinase-10/13 inhibitors via Dimroth rearrangement towards targeted polypharmacology, *Bioorg. Chem.* 96 (2020), 103616.
- [59] A. Vörös, Z. Baán, P. Mizsey, Z. Finta, Formation of aromatic amidoximes with hydroxylamine using microreactor Technology, *Org. Process Res. Dev.* 16 (2012) 1717–1726.
- [60] J. Lan, J. Ge, J. Yu, S. Shan, H. Zhou, S. Fan, Q. Zhang, X. Shi, Q. Wang, L. Zhang, Structure of the SARS-CoV-2 spike receptor-binding domain bound to the ACE2 receptor, *Nature* 581 (2020) 215–220.
- [61] H.A. Hassan, A.E. Allam, D.H. Abu-Baih, M.F.A. Mohamed, U.R. Abdelmohsen, K. Shimizu, S.Y. Desoukey, A.M. Hayallah, M.A. Elrehany, K.M. Mohamed, Isolation and characterization of novel acetylcholinesterase inhibitors from *Ficus benghalensis* L. leaves, *RSC Adv.* 10 (2020) 36920–36929.
- [62] M.I. Gadallah, H.R.H. Ali, H.F. Askal, G.A. Saleh, Towards understanding of the interaction of certain carbapenems with protein via combined experimental and theoretical approach, *Spectrochim. Acta Mol. Biomol. Spectrosc.* 246 (2021), 119005.
- [63] A.R. Khattab, M. Teleb, In silico discovery of non-psychoactive scaffolds in Cannabis halting SARS-CoV-2 host entry and replication machinery, *Future Virol.* 17 (2022) 367–386.
- [64] S.S. El Hawary, A.R. Khattab, H.S. Marzouk, A.S. El Senousy, M.G.A. Alex, O. M. Aly, M. Teleb, U.R. Abdelmohsen, In silico identification of SARS-CoV-2 spike (S) protein–ACE2 complex inhibitors from eight *Tecoma* species and cultivars analyzed by LC-MS, *RSC Adv.* 10 (2020) 43103–43108.
- [65] M.S. Ayoup, M.M. Abu-Serie, H. Abdel-Hamid, M. Teleb, Beyond direct Nrf2 activation; reinvestigating 1,2,4-oxadiazole scaffold as a master key unlocking the antioxidant cellular machinery for cancer therapy, *Eur. J. Med. Chem.* 220 (2021), 113475.
- [66] S. Houshmandfar, A. Saeedi-Boroujeni, M. Rashno, A. Khodadadi, M.-R. Mahmoudian-Sani, miRNA-223 as a regulator of inflammation and NLRP3 inflammasome, the main fragments in the puzzle of immunopathogenesis of different inflammatory diseases and COVID-19, *Naunyn-Schmiedeberg. Arch. Pharmacol.* 394 (2021) 2187–2195.
- [67] T. Mosmann, Rapid colorimetric assay for cellular growth and survival: application to proliferation and cytotoxicity assays, *J. Immunol. Methods* 65 (1983) 55–63.
- [68] W. Tai, L. He, X. Zhang, J. Pu, D. Voronin, S. Jiang, Y. Zhou, L. Du, Characterization of the receptor-binding domain (RBD) of 2019 novel coronavirus:

- implication for development of RBD protein as a viral attachment inhibitor and vaccine, *Cell. Mol. Immunol.* 17 (2020) 613–620.
- [69] W.-H. Chen, L. Du, S.M. Chag, C. Ma, N. Tricoche, X. Tao, C.A. Seid, E. M. Hudspeth, S. Lustigman, C.-T.K. Tseng, Yeast-expressed recombinant protein of the receptor-binding domain in SARS-CoV spike protein with deglycosylated forms as a SARS vaccine candidate, *Hum. Vaccines Immunother.* 10 (2014) 648–658.
- [70] O.T. No, 107: partition Coefficient (n-octanol/water): shake flask method, *OECD Guidelines for the Testing of Chemicals*, Section 1 (1995) 1.